Journal Pre-proofs

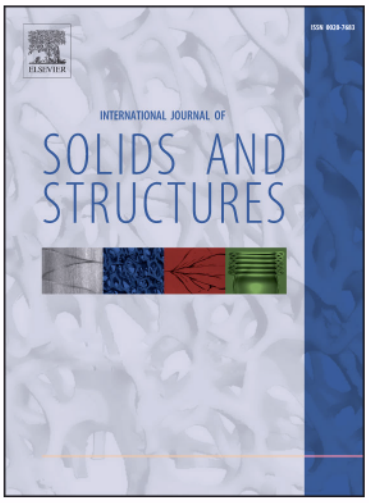

A non-isothermal breakage-damage model for plastic-bonded granular materials incorporating temperature, pressure, and rate dependencies

Yazeed Kokash, Richard Regueiro, Nathan Miller, Yida Zhang

PII: S0020-7683(24)00444-X
DOI: https://doi.org/10.1016/j.ijsolstr.2024.113085
Reference: SAS 113085

To appear in: *International Journal of Solids and Structures*

Received Date: 13 September 2024
Accepted Date: 23 September 2024

Please cite this article as: Kokash, Y., Regueiro, R., Miller, N., Zhang, Y., A non-isothermal breakage-damage model for plastic-bonded granular materials incorporating temperature, pressure, and rate dependencies, *International Journal of Solids and Structures* (2024), doi: https://doi.org/10.1016/j.ijsolstr.2024.113085

A non-isothermal breakage-damage model for plastic-bonded granular materials incorporating temperature, pressure, and rate dependencies

Yazeed Kokash[1], Richard Regueiro[2], Nathan Miller[3], Yida Zhang[2*]

Abstract

Plastic-bonded granular materials (PBM) are widely used in industrial sectors, including building construction, abrasive applications, and defense applications such as plastic-bonded explosives. The mechanical behavior of PBM is highly nonlinear, irreversible, rate dependent, and temperature sensitive governed by various micromechanical attributions such as grain crushing and binder damage. This paper presents a thermodynamically consistent, microstructure-informed constitutive model to capture these characteristic behaviors of PBM. Key features of the model include a breakage internal variable to upscale the grain-scale information to the continuum level and to predict grain size evolution under mechanical loading. In addition, a damage internal state variable is introduced to account for the damage, deterioration, and debonding of the binder matrix upon loading. Temperature is taken as a fundamental external state variable to handle non-isothermal loading paths. The proposed model is able to capture with good accuracy several important aspects of the mechanical properties of PBM, such as pressure-dependent elasticity, pressure-dependent yield strength, brittle-to-ductile transition, temperature dependency, and rate dependency in the post-yielding regime. The model is validated against multiple published datasets obtained from confined and unconfined compression tests, covering various PBM compositions, confining pressures, temperatures, and strain rates.

Keywords: Plastic-bonded explosives, Breakage, Damage, thermal effects, viscoplasticity

1. Introduction

Plastic-bonded granular materials (PBM) are composite materials that combine granular particles with a plastic binder and have numerous medical and industrial applications (Gonzalez-Gutierrez et al., 2018; Plassart et al., 2020; Rueda et al., 2017; Trzaskowska et al., 2023). A particular example of PBM are plastic-bonded explosives (PBX). They consist of crystals of energetic materials such as HMX (octahydro-1,3,5,7-tetranitro-1,3,5,5,7-tetrazocine) or TATB (1,3,5-triamino-2,4,6-trinitrobenzene) (Plassart et al., 2020), and a matrix of polymeric binder which can be either a thermoplastic or thermoset (Cady et al., 2006). To ensure safe handling, transportation, and storage of explosive materials, experimental examination of PBX must be accompanied by a solid theoretical understanding and reliable modeling and simulation techniques. Fundamental understanding of the thermomechanical response of PBX is also crucial in establishing their detonation characteristics, since the chemical kinetics of energetic

[1] PhD student, Department of Mechanical Engineering, University of Colorado Boulder, Boulder, Colorado, USA.
[2] Department of Civil, Environmental and Architectural Engineering, University of Colorado Boulder, Boulder, Colorado, USA.
[3] Center for National Security Initiatives, University of Colorado Boulder, Boulder, Colorado, USA.
*Corresponding author: yida.zhang@colorado.edu

materials depends on both the temperature and the mechanical states of the material (Clements and Mas, 2004; Idar et al., 1998).

Extensive experimental studies have been conducted to assess the mechanical, thermal, and chemical responses of PBM or PBX. These investigations encompassed various loading conditions and tests, such as quasi static uniaxial unconfined compression and tension tests (Funk et al., 1996; Gratton et al., 2009; Le et al., 2010; Manner et al., 2017; Plassart et al., 2020; Rae et al., 2002), triaxial compression tests (Gratton et al., 2009; Gruau et al., 2009; Le et al., 2010; Plassart et al., 2020; Wiegand and Reddingius, 2004; Wiegand and Reddingius, 2005; Wiegand et al., 2011), torsion tests (Gagliardi and Cunningham, 2009), dynamic tests (Cady et al., 2009; Jr et al., 2011; Xu et al., 2021) and fracture tests (Ferranti Jr et al., 2010; Liu et al., 2010; Liu et al., 2011; Plassart et al., 2020) for measuring stress-strain responses and fracture properties. Some Experiments have also included cyclic loading paths to explore the hysteretic, ratcheting, and fatigue mechanical behaviors of PBX (Buechler, 2013b; Le et al., 2010; Plassart et al., 2020). Data from triaxial tests (Gruau et al., 2009; Wiegand and Reddingius, 2004) indicate that the mechanical behavior of PBM is pressure dependent. Specifically, with increasing confining pressure, its strength and stiffness increases, and the post-yielding response transforms from strain softening (i.e., brittle) to hardening (i.e., ductile). These properties resemble those of granular materials like sands and granular rocks. Some tests were performed at various temperatures from -55 ºC to +80 ºC (Blumenthal et al., 2000; Clements, 2011; Gray III et al., 1998; Plassart et al., 2020). In general, experiments carried out on PBX at higher temperatures demonstrated a generally weaker and more ductile mechanical response. This was notable in the diminished stiffness of the stress-strain curves, reduced strength, and an increase in the strain at which the sample reached maximum stress. This is not surprising as polymeric binders are known to be temperature sensitive, i.e., their modulus and strength drops significantly above the glass-transition temperature. On the other hand, several studies (Cui et al., 2010; Gallagher et al., 2015; Li et al., 2020; Pereverzev and Sewell, 2020; Quansah et al., 2022) reported that the stiffness of pure explosive crystals like HMX also decreases with increasing temperature. It is therefore necessary to account for the temperature dependence of both the binder matrix and the energetic crystals in physics-based constitutive modeling of PBX. Finally, a number of experimental studies were conducted at a wide range of strain rates from 0.0001/s to 3000/s (Cady et al., 2009; Xu et al., 2021). The stress-strain curves of the overall PBX as well as the grains and the binders are found to be rate-dependent in both the elastic and the inelastic regimes (Cady et al., 2006; Wang et al., 2022; Zhang and Oskay, 2019), thus exhibiting combined viscoelasticity and viscoplasticity behaviors. Many constitutive models have been developed to describe the multi-faceted mechanical response of PBX (Bryant et al., 2023; Buechler, 2012, 2013a; Caliez et al., 2014; Gratton et al., 2009; Le, 2007; Le et al., 2010; Plassart et al., 2022; Zubelewicz et al., 2013). For example, Le et al. (2010) presented a model combining a damage-dependent isotropic hardening yield surface with Maxwell's viscoelastic model to account for rate effect. A viscoplastic model is proposed by Buechler (2012) for PBX 9501 and PBX 9502 that incorporates linear viscoelasticity, isotropic and kinematic rate-dependent hardening plasticity with a Drucker-Prager yield criterion. In Zubelewicz et al. (2013), a fracture-based viscoplastic model was proposed for PBX composites, which was calibrated for PBX-9502 and the model also included temperature effects. One of the most widely used constitutive model for the thermomechanical behavior of PBX is the Statistical CRAcks Mechanics model (SCRAM) (Dienes, 1996; Dienes et al., 2006; Dienes, 1978, 1985). It can capture the effect of "hot spots" in energetic materials that can originate not necessarily from thermal effects but from mechanical deformations. It takes into account the opening, growth, shear, and coalescence of cracks, plastic flow, and the nonlinear equation of state of the solid matrix. In addition, it considers the interfacial friction in closed cracks as a localization process that can lead to hot spots. Two simplified versions of SCRAM model have also been proposed later on which are the Iso-SCRAM and

visco-SCRAM models (Addessio and Johnson, 1990; Bennett et al., 1998). These simplified models assume that the distribution of cracks remains isotropic during deformation, as opposed to the original SCRAM model that considers the anisotropic nature of damage. A detailed comparison between the different constitutive models for PBX is summarized in Plassart et al. (2020).

Despite their excellent performance in capturing some aspects of the stress-strain characteristics of PBM, the majority of the existing constitutive models are phenomenological and thus do not track the microstructural evolution (e.g., grain breakage, binder matrix damage), nor mechanistically explain how these micro-scale attributions influence the overall macroscale behavior of PBM. In addition, many of these models lack a robust thermodynamic foundation and may thus not fully comply with the second law of thermodynamics under complex thermomechanical loading paths. Addressing these limitations is important for enhancing the accuracy and reliability in modeling PBM. In this context, the objective of this paper is twofold: 1) to develop a thermodynamic-consistent, microstructure-informed constitutive model for generic PBM under monotonic loading; 2) to comprehensively validate the model with published datasets encompassing the pressure, temperature, and rate dependent responses of PBX. The overall idea is to extend the Continuum Breakage-Damage Mechanics (CBDM) theory by Einav and co-workers (Das et al., 2014; Einav, 2007a, b; Tengattini et al., 2014) to model generic plastic-bonded granular materials, with specific application to PBX. We start by showing the derivation for a rate-independent non-isothermal CBDM model in Section 2. The generalization of the proposed model to include rate dependency is presented in Section 3. In Section 4, we demonstrate the performance of the proposed model by comparing with experimental data from literature in three different loading conditions: quasistatic triaxial compression, quasistatic compression at different temperatures and lastly, rate dependent behavior of the model at different strain rates. Finally, the main conclusions and possible future extensions of this work are discussed in Section 5.

2. Non-isothermal breakage-damage mechanics theory

2.1. Breakage and damage internal variables

Grain cracking and crushing are dominant during the irreversible deformation of PBM, as evidenced by in-situ X-ray images (Figure 1). The collective breakage of grains can be quantified by introducing a scalar internal state variable (ISV), namely the breakage (B) (Einav, 2007a, b). It is defined as $B \equiv B_c / B_t$ where B_c is the area enclosed by the initial and current grain size distributions (GSD) and B_t is the area between the initial and the final GSDs, as illustrated in Figure 2. Therefore, B=0 for initial unstressed specimens and B=1 for fully (ultimate) crushed samples. Assuming further that grain crushing is fractional independent (Einav, 2007a), the current cumulative GSD can be expressed as a linear interpolation between the initial and ultimate GSD with respect to B (Einav, 2007a):

$$F_c^g(d^g) = F_i^g(d^g)(1-B) + F_u^g(d^g)B \tag{1}$$

where F is the cumulative GSD by mass; d^g is grain diameter; subscripts i, u, c represent initial, ultimate, and current, respectively.

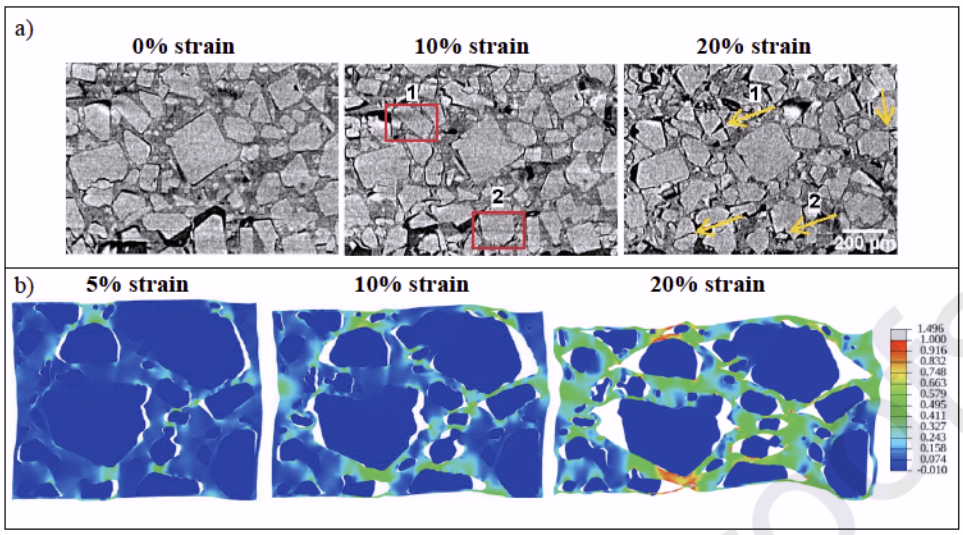

Figure 1: a) X-ray images from Manner et al. (2017) on a deforming HMX based PBX sample in a uniaxial compression test. Grain breakage is clearly observed through the course of loading; b) Finite element simulation of an energetic material under compression (Manner et al., 2017). Color contour indicates the accumulation of maximum principal strain within the binder matrix.

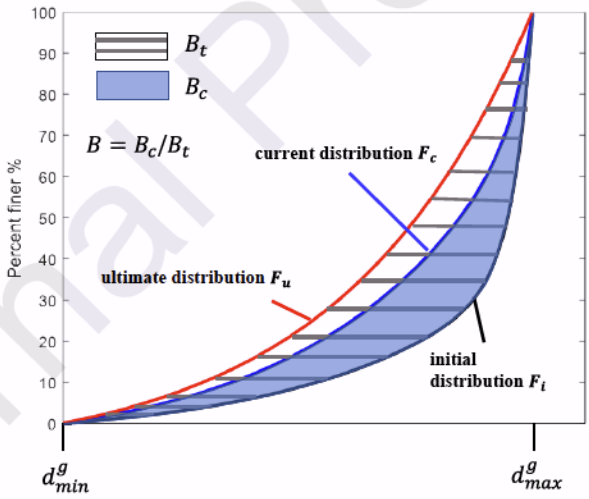

Figure 2: a) Definition of breakage based on grain size statistics (Einav, 2007a).

In Das et al. (2014) and Tengattini et al. (2014), a damage ISV was defined for brittle cemented granular geomaterials (e.g., sandstones) to account for the gradual cracking of the cement bridge that connects the grains due to loading. Specifically, whenever a cement bridge undergoes partial cracking, it is conceptually replaced with another bridge of undamaged material but with a smaller cross-sectional area. In PBM, the polymeric binder plays a similar role in maintaining cohesion between the grains, despite its relatively low quantity (approximately 5% by mass of the total material). We argue that the binder matrix experiences a similar damage process under stress. When the sample is sheared, the shear stress is transmitted through grain-to-grain friction as well as the grain-to-binder interfaces. As a result,

the binder matrix begins to accumulate damage and debonding from the grains, potentially enhancing the sliding, rotation, and crushing of the grains. The concept of binder damage finds support in meso-scale studies on PBM. For example, Manner et al. (2017) conducted finite element simulation of PBM with a grain-binder structure mapped from X-ray images, as depicted in Figure 1 (b). The results show that when the Representative Elementary Volume (REV) is being compressed and plastic deformation starts to accumulate in the binder, the grains initiate debonding from the matrix and reorganize and rotate. This suggests that the matrix binder, as load is being applied, starts to lose some of its functionality in terms of keeping cohesion between the grains and therefore, it is reasonable to introduce a damage ISV, D, to account for the deterioration and debonding of the binder matrix that can no longer supports the grains. Here we do not seek for a quantitative statistical measure to quantify D as done in Das et al. (2014) and Tengattini et al. (2014). Rather, we regard D as an overall measure of the ability of the binder matrix to provide cohesion to all the grains at the REV level, with $D = 0$ being the intact and healthy binder matrix, and $D = 1$ representing the complete detachment of the grain and the binder. In summary, the damage of the binder represents the debonding of the grain/binder interface micromechanism and any other dissipative micromechanism that ultimately reduces the total binder stiffness and the overall cohesion provided to the whole material system.

2.2. Non-isothermal CBDM theory

The first and the second laws of thermodynamics for a deforming material REV under non-isothermal condition is given by (Houlsby and Puzrin, 2007)

$$\dot{\Psi} + \tilde{\Phi} = \sigma_{ij}\dot{\varepsilon}_{ij} - S\dot{T}, \ \ \tilde{\Phi} \geq 0 \tag{2}$$

where σ_{ij} and ε_{ij} are respectively the stress and strain tensors for small strain theory, with compression being defined as positive (i.e., the *soil mechanics* sign convention) (Houlsby and Puzrin, 2007); S is the entropy; T is the temperature; Ψ is the Helmholtz free energy or elastic strain energy of the solid and should be a function of elastic strain, temperature, and ISVs, i.e., $\Psi = \Psi(\varepsilon_{ij}^{e}, T, B, D)$; $\tilde{\Phi}$ is the dissipation rate function and will depend on the irreversible rates such as the plastic strain, breakage, and damage rates, i.e., $\tilde{\Phi} = \tilde{\Phi}(\dot{\varepsilon}_{ij}^{p}, \dot{B}, \dot{D})$; Superscripts e and p denote elastic and plastic, respectively; the dot "$\bullet$" above a variable X indicates the time rate of change of X.

Assuming that $\tilde{\Phi}$ is a homogenous first-order function in the rates $\dot{\varepsilon}_{ij}^{p}$, $\dot{B}$, and $\dot{D}$, which is necessary to describe the quasi-static rate-independent behavior for hyperplastic materials (Houlsby and Puzrin, 2007), we can write the following

$$\dot{\Psi} = \sigma_{ij}\dot{\varepsilon}_{ij}^{e} - S\dot{T} - E_B\dot{B} - E_D\dot{D} \tag{3}$$

$$\tilde{\Phi} = \overline{\sigma}_{ij}\dot{\varepsilon}_{ij}^{p} + \overline{E}_B\dot{B} + \overline{E}_D\dot{D} \tag{4}$$

where

$$\sigma_{ij} = \frac{\partial\Psi}{\partial\varepsilon_{ij}^{e}}; \ E_B = -\frac{\partial\Psi}{\partial B}; E_D = -\frac{\partial\Psi}{\partial D}; S = -\frac{\partial\Psi}{\partial T} \tag{5}$$

are the true stress, breakage energy, damage energy, and entropy, respectively; and

$$\bar{\sigma}_{ij} = \frac{\partial \tilde{\Phi}}{\partial \dot{\varepsilon}_{ij}^{p}}, \bar{E}_B = \frac{\partial \tilde{\Phi}}{\partial \dot{B}}, \bar{E}_D = \frac{\partial \tilde{\Phi}}{\partial \dot{D}} \tag{6}$$

are defined as the dissipative stress, dissipative breakage energy, and dissipative damage energy, respectively. The bar symbol is used to distinguish between the true and the dissipative quantities. The dissipative stresses are introduced to serve as the *thermodynamic force* that is conjugate to the ISV rates in the dissipation rate function, similar to true stresses being the thermodynamic force of the state variables for the free energy potential (Houlsby and Puzrin, 2007). This concept may be circumvented if one accepts a priori that the thermodynamic forces for energy dissipation and energy storage are identical. However, we found that dissipative stresses are necessary to simplify the generalization of a quasi-static hyperplastic model to a rate-dependent one through the so-called flow and force potentials (Zhang and Buscarnera, 2017), as shall be seen in Section 3. Combining Eqs. (2), (3) and (4), and accepting Ziegler's orthogonality rule, one obtains:

$$\sigma_{ij} = \bar{\sigma}_{ij}; E_B = \bar{E}_B; E_D = \bar{E}_D \tag{7}$$

Eq. (7) is useful in expressing the final constitutive equations in the true stress space after the model is deduced from the proposed scalar functions Ψ and $\tilde{\Phi}$, following the hyperplasticity procedure.

The explicit expressions of Ψ and $\tilde{\Phi}$ should be highly material specific and proposed closely pertaining to the underlying physical reality. For PBM, the Helmholtz free energy will be a contribution of both the grains and binder. Inspired by the previous works of Einav and co-workers (Einav, 2007a, b; Tengattini et al., 2014), the total free energy considering both contributions and non-isothermal condition is proposed as

$$\begin{aligned} \Psi\left(\varepsilon_{ij}^{e}, B, D, T\right) &= \Psi^{g}\left(\varepsilon_{ij}^{e}, B, T\right) + \Psi^{b}\left(\varepsilon_{ij}^{e}, D, T\right) \\ &= \left(1-\vartheta B\right)\phi^{g}\,\psi_{r}^{\,g}\left(\varepsilon_{ij}^{e}, T\right) + \left(1-D\right)\phi^{b}\,\psi_{r}^{\,b}\left(\varepsilon_{ij}^{e}, T\right) \end{aligned} \tag{8}$$

where ϑ is the grading index which is determined by the knowledge of the initial and ultimate grain size distributions; ψ_r is the reference free energy; ϕ is the volume fraction; superscripts *g* and *b* denote grain and binder, respectively.

Most of the existing PBM experimental datasets are obtained from axisymmetric specimens (i.e., cylinders). It is therefore convenient to limit the remainder of the model development to the triaxial space. Substituting Eq. (8) into Eq. (5), we have

$$p = \frac{\partial \Psi}{\partial \varepsilon_{v}^{e}} = \left(1-\vartheta B\right)\phi^{g}\frac{\partial \psi_{r}^{\,g}}{\partial \varepsilon_{v}^{e}} + \left(1-D\right)\phi^{b}\frac{\partial \psi_{r}^{\,b}}{\partial \varepsilon_{v}^{e}} \tag{9}$$

$$q = \frac{\partial \Psi}{\partial \varepsilon_{s}^{e}} = \left(1-\vartheta B\right)\phi^{g}\frac{\partial \psi_{r}^{\,g}}{\partial \varepsilon_{s}^{e}} + \left(1-D\right)\phi^{b}\frac{\partial \psi_{r}^{\,b}}{\partial \varepsilon_{s}^{e}} \tag{10}$$

$$E_B = -\frac{\partial \Psi}{\partial B} = \vartheta \phi^g {\psi_r}^g \tag{11}$$

$$E_D = -\frac{\partial \Psi}{\partial D} = \phi^b {\psi_r}^b \tag{12}$$

$$S = -\frac{\partial \Psi}{\partial T} = -\left((1-\vartheta B)\phi^g \frac{\partial {\psi_r}^g}{\partial T} + (1-D)\phi^b \frac{\partial {\psi_r}^b}{\partial T} \right) \tag{13}$$

where p and q are respectively the mean and deviatoric stresses; ε_v and ε_s are respectively the volumetric and deviatoric strains.

Under mechanical loading, there are three primary energy dissipation mechanisms for PBM, as illustrated in Figure 3. These mechanisms include grain breakage, binder damage, and plastic dissipation. Plastic dissipation consists of both volumetric and shear components. The volumetric dissipation accounts for grain reorganization (to form a denser packing), while the shear component captures the frictional interactions among compressed grains. These mechanisms are highly coupled and occur simultaneously throughout the deformation process. Therefore, a coupled dissipation rate function is used:

$$\tilde{\Phi}\left(\dot{\varepsilon}_v^p, \dot{\varepsilon}_s^p, \dot{B}, \dot{D}\right) = \sqrt{\left(\tilde{\Phi}_{pv}\left(\dot{\varepsilon}_v^p\right)\right)^2 + \left(\tilde{\Phi}_{ps}\left(\dot{\varepsilon}_s^p\right)\right)^2 + \left(\tilde{\Phi}_B\left(\dot{B}\right)\right)^2 + \left(\tilde{\Phi}_D\left(\dot{D}\right)\right)^2} \tag{14}$$

where $\tilde{\Phi}_{pv}$, $\tilde{\Phi}_{ps}$, $\tilde{\Phi}_B$, and $\tilde{\Phi}_D$ are the volumetric, shear, breakage, and damage dissipation rates, respectively.

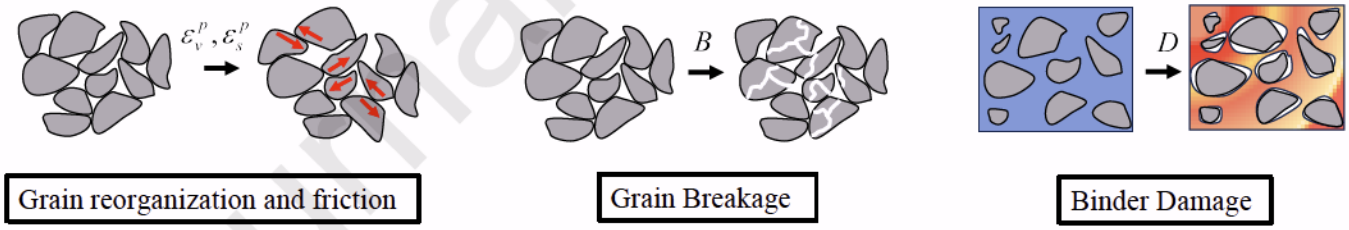

Figure 3: Dissipation mechanisms in the model, including volumetric and shear plastic strains, representing grains reorganization and friction between the grains, as well as breakage of the grains and damage to the binder matrix.

Performing Legendre transformation of Eq. (14), one can obtain a function expressed in terms of the thermodynamics forces $\bar{y}\left(\bar{p}, \bar{q}, \bar{E}_B, \bar{E}_D\right) \le 0$, which defines the yield surface of the resultant elastoplastic model:

$$\bar{y}\left(\bar{p},\bar{q},\bar{E}_B,\bar{E}_D\right)=\left(\frac{\bar{E}_B}{\frac{\partial\tilde{\Phi}_B}{\partial\dot{B}}}\right)^2+\left(\frac{\bar{E}_D}{\frac{\partial\tilde{\Phi}_D}{\partial\dot{D}}}\right)^2+\left(\frac{\bar{p}}{\frac{\partial\tilde{\Phi}_{pv}}{\partial\dot{\varepsilon}_v^p}}\right)^2+\left(\frac{\bar{q}}{\frac{\partial\tilde{\Phi}_{ps}}{\partial\dot{\varepsilon}_s^p}}\right)^2-1\le 0 \tag{15}$$

The inelastic flow rules immediately follow:

$$\dot{\varepsilon}_v^p=\dot{\lambda}\frac{\partial\bar{y}}{\partial\bar{p}};\dot{\varepsilon}_s^p=\dot{\lambda}\frac{\partial\bar{y}}{\partial\bar{q}};\dot{B}=\dot{\lambda}\frac{\partial\bar{y}}{\partial\bar{E}_B};\dot{D}=\dot{\lambda}\frac{\partial\bar{y}}{\partial\bar{E}_D} \tag{16}$$

where $\dot{\lambda}\ge 0$ is the plastic multiplier which can be determined by enforcing the consistency condition.

It is possible to combine the incremental form of the elastic relation Eq. (5), the yield surface (15), the flow rule (16), and the strain decomposition $\varepsilon_{ij}=\varepsilon_{ij}^e+\varepsilon_{ij}^p$ to eliminate $\dot{\lambda}$ and arrive at the following incremental constitutive relation (see Appendix A):

$$\begin{pmatrix}\dot{p}\\ \dot{q}\\ \dot{S}\end{pmatrix}=\left[\mathbf{D}^e-\mathbf{D}^p-\mathbf{D}^B-\mathbf{D}^D\right]\begin{pmatrix}\dot{\varepsilon}_v\\ \dot{\varepsilon}_s\\ \dot{T}\end{pmatrix} \tag{17}$$

where $\mathbf{D}^e,\mathbf{D}^p,\mathbf{D}^B$, and $\mathbf{D}^D$ are the elastic, plastic, breakage, and damage contributions to the constitutive response, respectively. Eq. (17) is the general form of a non-isothermal breakage-damage mechanics model for plastic bonded materials. Considering most experimental data on PBM are obtained at isothermal condition (although at different temperatures), we exercise a simplified version of Eq. (17) under $\dot{T}=0$. For the same reason, we will not discuss the entropy evolution, and instead focus on the response of the model in terms of stress-strain-breakage-damage evolutions at different constant temperatures.

2.3. A specific CBDM model

Recent confined triaxial compression tests conducted on PBM have revealed a compression response that depends on the applied pressure (Gruau et al., 2009; Wiegand and Reddingius, 2004; Wiegand and Reddingius, 2005). Similar pressure-dependent behaviors have been observed in other granular materials as well. Therefore, it is necessary to consider a pressure-dependent bulk modulus for the grains, while assuming a linear elastic model for shear deformation. In contrast, the binder in this formulation is assumed to have linear elastic moduli for both the bulk and shear responses. This assumption is supported by experimental data demonstrating a linear stress-strain response within the binder elastic range (Cady et al., 2006). According to the above, the reference Helmholtz free energy for the grain and the binder are proposed as

$$\psi_r^g\left(\varepsilon_v^e,\varepsilon_s^e,T\right)=\frac{2}{3}\frac{p_r}{\overline{K}^g}\left\{\frac{\overline{K}^g}{2}\left[\varepsilon_v^e-3\alpha^g(T-T_0)\right]+1\right\}^3+\frac{3}{2}G^g\varepsilon_s^{e2}-\frac{C^g}{T_0}\frac{(T-T_0)^2}{2} \tag{18}$$

$$\psi_r^b\left(\varepsilon_v^e,\varepsilon_s^e,T\right)=\frac{1}{2}K^b\varepsilon_v^{e2}+\frac{3}{2}G^b\varepsilon_s^{e2}-3\alpha^bK^b(T-T_0)\varepsilon_v^e-\frac{C^b}{T_0}\frac{(T-T_0)^2}{2} \tag{19}$$

where $\overline{K}^g$ and G^g are the elastic parameters of the grains and K^b and G^b are the elastic constants of the binder matrix; p_r is a reference pressure usually taken as 1 kPa; T_0 is the initial temperature; α is the linear thermal expansion coefficient; C is the heat capacity. Eq. (18) embodies a pressure-dependent elasticity model and (19) corresponds to a linear elasticity model. Note that the material parameters such as K and G should also be functions of the temperature. Their expressions shall be decided based on experimental data, as discussed later. Substituting Eqs. (18) and (19) in Eq. (8), the total Helmholtz free energy becomes

$$\begin{aligned}\Psi\left(\varepsilon_v^e,\varepsilon_s^e,T,B,D\right)=&\underbrace{(1-\vartheta B)\phi^g\left\{\frac{2}{3}\frac{p_r}{\overline{K}^g}\left\{\frac{\overline{K}^g}{2}\left[\varepsilon_v^e-3\alpha^g(T-T_0)\right]+1\right\}^3+\frac{3}{2}G^g\varepsilon_s^{e2}-\frac{C^g}{T_0}\frac{(T-T_0)^2}{2}\right\}}_{grains}\\&+\underbrace{(1-D)\phi^b\left[\frac{1}{2}K^b\varepsilon_v^{e2}+\frac{3}{2}G^b\varepsilon_s^{e2}-3\alpha^bK^b(T-T_0)\varepsilon_v^e-\frac{C^b}{T_0}\frac{(T-T_0)^2}{2}\right]}_{binder}\end{aligned} \tag{20}$$

Substituting (20) into (5), one obtains the elastic relations as

$$p=(1-\vartheta B)\phi^g p_r\left\{\frac{\overline{K}^g}{2}\left[\varepsilon_v^e-3\alpha^g(T-T_0)\right]+1\right\}^2+(1-D)\phi^bK^b\left[\varepsilon_v^e-3\alpha^b(T-T_0)\right] \tag{21}$$

$$q=3(1-\vartheta B)\phi^gG\varepsilon_s^e+3(1-D)\phi^bG^b\varepsilon_s^e \tag{22}$$

$$E_B=\vartheta\phi^g\left\{\frac{2}{3}\frac{p_r}{\overline{K}^g}\left\{\frac{\overline{K}^g}{2}\left[\varepsilon_v^e-3\alpha^g(T-T_0)\right]+1\right\}^3+\frac{3}{2}G^g\varepsilon_s^{e2}-\frac{C^g}{T_0}\frac{(T-T_0)^2}{2}\right\} \tag{23}$$

$$E_D=\phi^b\left[\frac{1}{2}K^b\varepsilon_v^{e2}+\frac{3}{2}G^b\varepsilon_s^{e2}-3\alpha^bK^b(T-T_0)\varepsilon_v^e-\frac{C^b}{T_0}\frac{(T-T_0)^2}{2}\right] \tag{24}$$

The dissipation rate functions are proposed as follows, based on the previous works of Einav (2007b), Shen and Buscarnera (2022), and Tengattini et al. (2014):

$$\begin{aligned}
\tilde{\Phi}_{pv} &= \frac{p}{\sqrt{\dfrac{E_B(1-B)^{s_B}\sin^2(\omega_B)}{E_{BC}} + \dfrac{E_D(1-D)^{s_D}\sin^2(\omega_D)}{E_{DC}}}}\dot{\varepsilon}_v^p \\
\tilde{\Phi}_{ps} &= \left[M^* p^n p_r^{(1-n)} + c(1-D)\right]\dot{\varepsilon}_s^p \\
\tilde{\Phi}_B &= \frac{\sqrt{E_B E_{BC}}}{(1-B)^{s_B}\cos(\omega_B)}\dot{B} \\
\tilde{\Phi}_D &= \frac{\sqrt{E_D E_{DC}}}{(1-D)^{s_D}\cos(\omega_D)}\dot{D}
\end{aligned} \tag{25}$$

Eq. (25) obviously guarantees Eq. (14) to be a first-order homogenous function that satisfies Eq. (4). E_{BC} and E_{DC} are the breakage and damage critical energies that control the size of the yield surface of the material. The critical breakage energy marks the limit at which the grains start to crush and break while the critical damage energy indicates when the binder-grain interfaces start to accumulate damage and the grains then start to slide and detach. Compared to Tengattini et al. (2014), two new parameters s_B and s_D are introduced to control the growth rate of breakage and damage after yielding. The added flexibility of s_B is demonstrated in our previous work (Singh et al., 2021). M^* characterizes the critical stress ratio q/p after the material is sheared to steady state. Since the grains are bonded together using a matrix of binder, it is expected that cohesion exists but will diminish as damage accumulates. Parameter c characterizes the initial cohesion of the pristine material. Finally, ω_B and ω_D are the coupling angles controlling the relative contribution of breakage and damage dissipations during the inelastic deformation. The pressure-dependent frictional dissipation is controlled by parameter n in the $\tilde{\Phi}_{ps}$ expression which embodies the Hoek-Brown failure envelope (Das et al., 2011). Substituting Eq. (25) into Eq. (15) and enforcing Eq. (7) gives the yield surface in true stress space

$$y(p,q,B,D,E_B,E_D) = \frac{E_B}{E_{BC}}(1-B)^{s_B} + \frac{E_D}{E_{DC}}(1-D)^{s_D} + \left(\frac{q}{M^* p^n p_r^{(1-n)} + c(1-D)}\right)^2 - 1 \le 0 \tag{26}$$

2.4. Model behavior

Figure 4 (a) shows the typical stress strain curves predicted by the model under triaxial compression at confining pressures from low to high. Table 1 lists the parameters selected in this set of simulations. They are arbitrarily selected bounded by their typical ranges for brittle granular materials based on the authors' past experience. The figure shows a softening effect at lower confining pressures (5 and 30 MPa) followed by a transition to strain hardening as the confining pressure increases (80 and 150 MPa), for the selected set of parameters. The model also demonstrates its ability to capture pressure-dependent elasticity and failure. These behaviors are characteristic of granular soils and cemented granular rocks (Donaghe et al., 1988; Wong and Baud, 2012), as well as real and mock PBX (Le et al., 2010; Wiegand and Reddingius, 2004). Figure 4 (b) depicts the evolution of breakage and damage variables for confining pressures of 5

and 150 MPa. Notably, the breakage and damage values for the 5 MPa confining pressure are lower compared to the 150 MPa confining pressure. This aligns with expectations since higher confining pressures result in elevated stress levels, consequently leading to increased breakage and damage. Finally, it is noteworthy that the predicted evolution of damage progresses more rapidly than the growth of breakage under both confining pressures. This can be attributed to the specific parameter settings employed in this case, where the critical damage energy is lower than the critical breakage energy (specifically, half the value of the critical breakage energy).

Table 1: Parameters used for different model predictions.

Figure	$\bar{K}^g$	G^g	K^b	G^b	E_{BC}	E_{DC}	M^*	n	c	ω_B	ω_D	s_B	s_D	ϑ	η	m
	-	MPa	MPa	MPa	MPa	MPa	-	-	MPa	^{o}	^{o}	-	-	-	s	-
Figure 4	25000	4000	16000	3500	3	1.5	1.5	1	40	45	45	2	2	0.95	-	-
Figure 7	7934.35	3244.81	3571.05	49.32	6.03	0.07	15.67	0.75	4	22.87	1.10	2	2	0.92	-	-
Figure 11	36163.12	3162.64	2609.84	74.80	0.07	0.0166	88.46	0.58	5	83.97	0	3.24	2	0.1	-	-
Figure 12																
T = -40 ^oC	1440.19	4045.11	365.49	168.69	9.63	0.0315	0.96	1	5.85	60.26	52.18	2	2	0.34	-	-
T = -15 ^oC	1200.20	1435.29	308.74	142.50	4.04	0.0122	0.96	1	2.87	60.26	52.18	2	2	0.34	-	-
T = 23 ^oC	1130.59	935.94	240.66	111.07	3.60	0.0057	0.96	1	1.79	60.26	52.18	2	2	0.34	-	-
T = 55 ^oC	1020.11	615.11	68.78	31.75	1.14	0.0027	0.96	1	1.43	60.26	52.18	2	2	0.34	-	-
Figure 14																
T = -10 ^oC	8582.31	3968.88	2097.39	879.57	14.27	0.0418	0.71	1	38.56	53.82	78.28	2	2	0.73	-	-

$T = 25\,^{o}C$	6607.98	1681.60	614.37	257.70	7.81	0.0156	0.71	1	14.86	53.82	78.28	2	2	0.73	-	-
$T = 74\,^{o}C$	4063.16	896.91	142.96	59.96	1.75	0.0063	0.71	1	9.77	53.82	78.28	2	2	0.73	-	-
Figure 15	1330	2000	460	130.95	2.084	0.0018	0.62	1	1.98	79.87	57.56	4.33	3.33	0.26	20	1.8

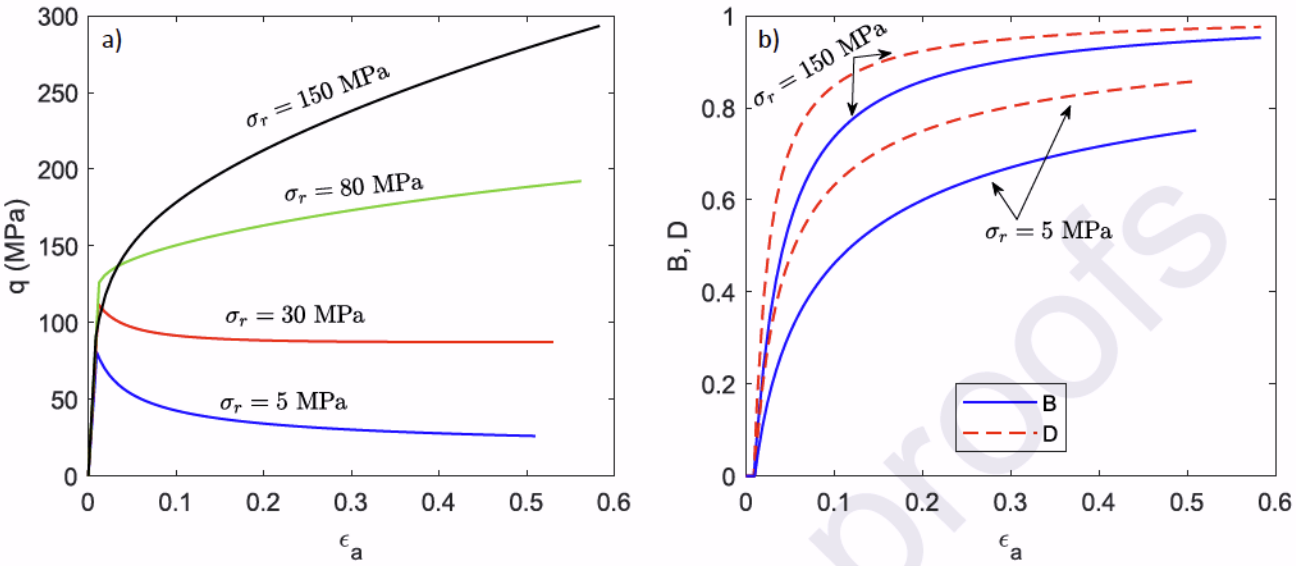

Figure 4: a) Deviatoric stress (q) vs axial strain (ε_a) for four confining pressures (5, 30, 80, and 150 MPa). There is softening at lower confining pressures, specifically 5 and 30 MPa, followed by a transition to strain hardening as the confining pressure increases; b) evolution of breakage and damage internal variables for the 5 and 150 MPa. The evolution of breakage and damage exhibits faster rates of change during the early stages of loading for both the 5 and 150 MPa cases. However, as loading progresses, the rates of evolution gradually decrease.

Figure 5 shows the progressive evolution of the yield surfaces for confining pressures of 5 and 150 MPa. Below certain mean stress (for the selected set of parameters, around 55 MPa), the yield surfaces exhibit rapid contraction after the initial yielding, resulting in strain softening. At higher mean stresses, the yield surface expands, producing a strain-hardening response. This is known as brittle-ductile transition in rock mechanics literature, with localized failure (e.g., splitting, fracturing) being expected in the low-stress brittle regime and diffused failure pattern expected in the high-stress ductile regime (Paterson and Wong, 2005). Note that the cohesion (the intersection between the yield locus and the q-axis) reduces for both cases as loading progresses. This is caused by the accumulation of D and thus the reduction of apparent cohesion $c(1-D)$ in Eq. (26). In addition, it is understood that the full prediction of the softening, localized failure of PBM at low confining pressures in an initial-boundary-value-problem setting (e.g., in finite element simulations) may require additional model enrichments to remove the mesh dependency and to account for additional microstructural couplings. Methods such as non-local or strain gradient (Bazant et al., 1984), micropolar (Collins-Craft et al., 2020), micromorphic (Miller et al., 2022; Regueiro, 2010), and viscoplastic regularizations (Das et al., 2013) may be integrated into the model in future extensions.

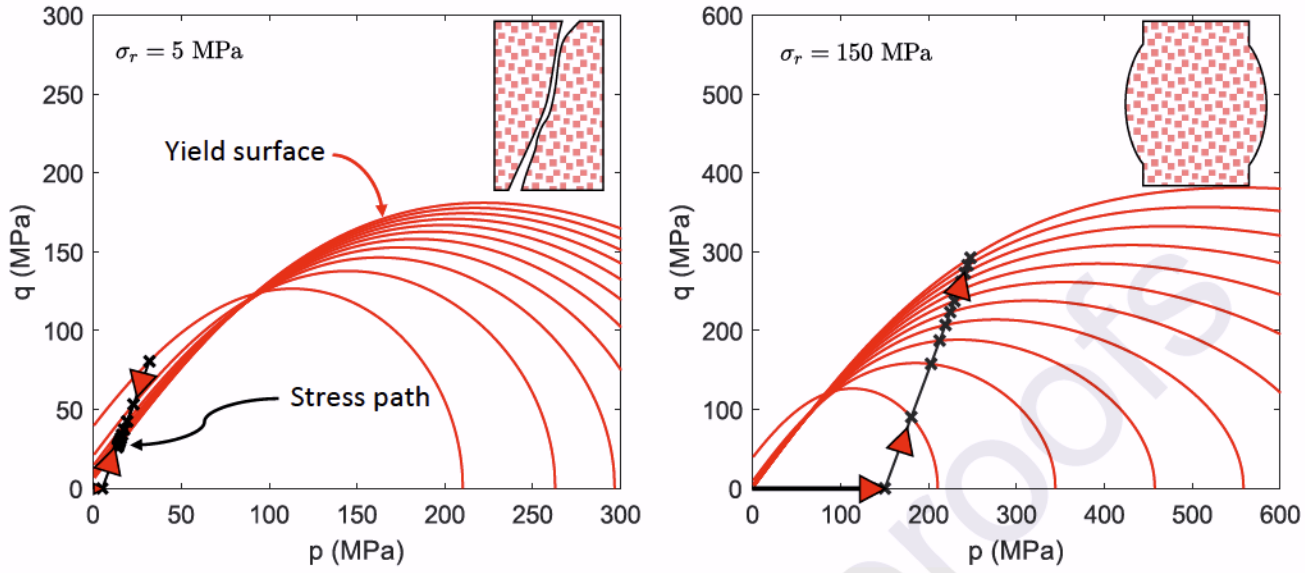

Figure 5: The evolution of yield surfaces for the 5 and 150 MPa cases. At low confining pressures, the yield surfaces contract, whereas at high confining pressures, they expand. For low confining pressure, the expected failure mode is brittle fracture as depicted by the sketch on the left. Meanwhile, for high confining pressure, the sample usually fails in a bulging form as depicted in the sketch on the right. The stress path is depicted by the black lines.

3. Rate-dependent generalization

Before applying CBDM for real PBM which are characterized by salient rate-dependent behaviors (Cady et al., 2009; Xu et al., 2021), it is necessary to generalize the basic quasi-static model in Section 2 with rate-dependency. This can be achieved by considering a higher-order homogeneous or non-homogeneous dissipation rate function $\tilde{\Phi}$, or equivalently, by introducing a *flow potential* w or a *force potential* z, as systematically discussed in Houlsby and Puzrin (2007) and Zhang and Buscarnera (2017). According to these works, the relations between the force potential, flow potential, and the dissipation rate functions are given as:

$$w(\mathbf{A},\overline{\boldsymbol{\chi}}) = \overline{\boldsymbol{\chi}} : \dot{\boldsymbol{\alpha}} - z = \tilde{\Phi} - z\,, \quad z(\mathbf{A},\dot{\boldsymbol{\alpha}}) = \int_0^1 \frac{\tilde{\Phi}(\mathbf{A},\tau\dot{\boldsymbol{\alpha}})}{\tau}\mathrm{d}\tau \text{, and } \tilde{\Phi}(\mathbf{A},\dot{\boldsymbol{\alpha}}) = \frac{\partial z}{\partial \dot{\boldsymbol{\alpha}}} : \dot{\boldsymbol{\alpha}} \tag{27}$$

where $\mathbf{A}$ is the set of external variables (the elastic strains for example); $\dot{\boldsymbol{\alpha}}$ is the set of internal variables rate ($\dot{B}$ for example); $\overline{\boldsymbol{\chi}}$ is the corresponding thermodynamic forces; τ is a dummy variable. Given a flow potential w, the evolution laws of the plastic strain, breakage, and damage can be obtained by

$$\dot{\varepsilon}_v^p = \frac{\partial w}{\partial \overline{p}}; \dot{\varepsilon}_s^p = \frac{\partial w}{\partial \overline{q}}; \dot{B} = \frac{\partial w}{\partial \overline{E}_B}; \dot{D} = \frac{\partial w}{\partial \overline{E}_D} \tag{28}$$

Here, we propose the following form of the flow potential inspired by the rate-dependent breakage mechanics formulation of Zhang and Buscarnera (2017),

$$w(\overline{p},\overline{q},\overline{E}_B,\overline{E}_D)=\frac{\sqrt{E_{BC}E_{DC}}}{\eta}\frac{\overline{\xi}^m}{m} \tag{29}$$

where $\overline{\xi}=\langle\overline{y}\rangle$ is the overstress function that measures the extent that the stress state surpasses the current yield surface; $\overline{y}$ is identical to Eq. (15); $\langle\bullet\rangle$ is the Macauley bracket; η is a viscosity parameter with a unit of [time]; and m is an exponent that controls the nonlinear effect in the rate dependency. In Zhang and Buscarnera (2017), this parameter is motivated from the physics of subcritical crack growth and is termed as the corrosion index. The introduction of the pre-factor $\sqrt{E_{BC}E_{DC}}/\eta$ in this structure ensures that the unit of the inelastic rates is correct, i.e., [1/time]. Combining Eqs. (28) and (29), the flow rules can be expressed in true stress space (after enforcing Eq. (7)) as

$$\begin{aligned}
\dot{\varepsilon}_v^p &= \frac{2\sqrt{E_{BC}E_{DC}}}{\eta p}\left[\frac{E_B(1-B)^{s_B}\sin^2(\omega_B)}{E_{BC}}+\frac{E_D(1-\mathrm{D})^{s_D}\sin^2(\omega_D)}{E_{DC}}\right]\xi^{m-1}\\
\dot{\varepsilon}_s^p &= \frac{2\sqrt{E_{BC}E_{DC}}\,q}{\eta\left[Mp^n p_r^{1-n}+c(1-\mathrm{D})\right]^2}\xi^{m-1}\\
\dot{B} &= \frac{2\sqrt{E_{BC}E_{DC}}(1-B)^{s_B}\cos^2(\omega_B)}{\eta E_{BC}}\xi^{m-1}\\
\dot{D} &= \frac{2\sqrt{E_{BC}E_{DC}}(1-D)^{s_D}\cos^2(\omega_D)}{\eta E_{DC}}\xi^{m-1}
\end{aligned} \tag{30}$$

where $\xi=\langle y\rangle$ is the overstress function in the true stress space. Observing Eq. (30), one can see that the role of flow potential Eq. (29) is to realize a Perzyna-type viscoplastic generalization of rate-independent models, with the rate of inelastic evolution decided by the overstress (Perzyna, 1966).

To examine the performance of the rate-dependent model, we simulate again the triaxial compression test under the 5 MPa confining pressure at various strain rates (1×10^{-6}, 0.1, 0.5, and 1 /s,) with rate parameters $\eta=0.1$ and $m=0.2$, and keeping the same mechanical parameters as those used for Figure 4. The results are plotted in Figure 6. It is observed that the stress-strain curve produced by the rate-dependent model converges to that of the rate-independent version (Section 2) at extremely low strain rate (1×10^{-6}/s). With an increase in strain rate, both shear strength and post-yielding stresses increases, mirroring the behavior commonly observed in PBM (Clements, 2011; Funk et al., 1996; Plassart et al., 2020). The effect of the two rate parameters (η and m) on the predicted stress-strain, creep, and relaxation responses at different strain rates is demonstrated in our previous works (Zhang and Buscarnera, 2017).

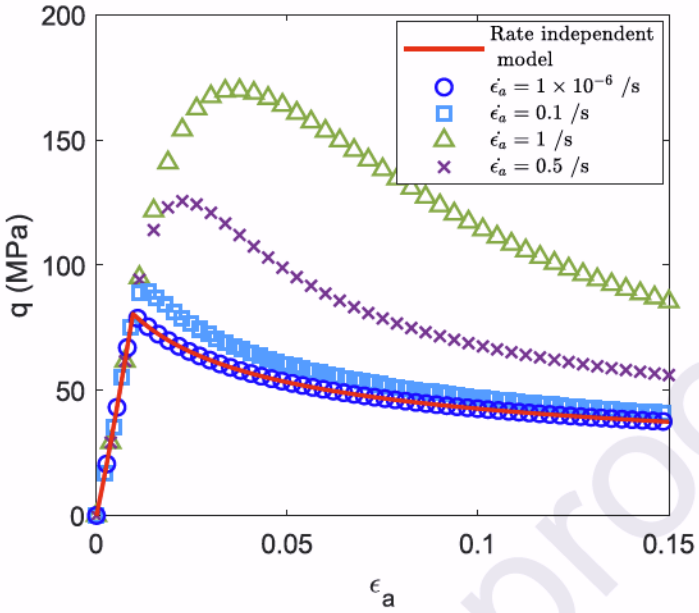

Figure 6: Rate-dependent model for drained triaxial compression under 5 MPa confining pressure at different strain rates. At $\dot{\varepsilon}_a = 1\times10^{-6}$, the rate-dependent model curve is identical to the rate-independent model.

4. Model Performance

4.1. Quasi-static triaxial compression tests on PBX-9501

First, we test the performance of the model against the quasi-static triaxial compression dataset on a mock explosive PBS-9501 (Wiegand and Reddingius, 2005). This material comprises granular sugar and a BDNPA/estane binder (Funk et al., 1996). PBS-9501 was specifically developed as a mock for the well-known PBX-9501 which is an HMX-based PBX. The experiments were carried out under varying confining pressures, ranging from 3.4 MPa to 138 MPa. Their dataset also includes an unconfined compression curve for this material.

The strategy for performance assessment is the following: First, we pick three curves, namely the unconfined compression (0 MPa), the 34 MPa, and the 138 MPa confining pressure stress-strain curves for model calibration. The calibrated parameters will then be used to predict the material responses under other confining pressures (3.4, 6.9, 17, 69 MPa) and compared with the experimental results to evaluate the model predictive capability. All simulations, except section 4.4, are performed using the rate-independent model. Temperature is fixed at room temperature in this series of tests, therefore we set $T=T_0$ and $\mathrm{d}T = 0$ in the simulation. In the triaxial compression simulations, the process consists of two stages. The initial stage involves isotropic compression, wherein the sample undergoes pressurization from all sides until reaching a predetermined confining pressure. Subsequently, axial strain is applied in the second stage of the test to introduce shearing while holding the confining pressure constant.

A global optimization technique was employed for the calibration step. The renowned robust "Genetic algorithm" was used to obtain the model parameters (Gen and Cheng, 1999; Goldberg and Holland, 1988). The built-in function in MATLAB "ga" was used. Briefly, the optimization process is to

minimize $F\left(\vec{p}\right)$ subjected to $\vec{lb} \le \vec{p} \le \vec{ub}$, where $F\left(\vec{p}\right) = \sum_i norm_i = \sum_i \sqrt{\left(q_i^{\text{model}} - q_i^{\text{experiment}}\right)^2}$ is the objective function; q^{model} and $q^{experiment}$ are the deviatoric stress obtained from the simulation and the experiments, respectively; $\vec{p}$ is the parameters vector which are the parameters listed in Table 1; $\vec{lb}$ and $\vec{ub}$ are the lower and upper bound vectors for the parameters used in the optimization. Since we used three curves for the objective function, the objective function was the sum of the norm error of the three curves. The best values for the parameters were obtained and are listed in Table 1. The lower and upper bounds for the optimization process were chosen based on values reported in the literature and through manual calibration. After having a rough idea of the values of these parameters, we set the lower and upper bounds with reasonable range to give the optimizer sufficient flexibility.

All curves and experimental data are plotted in Figure 7. The proposed model demonstrates remarkable accuracy in predicting the mechanical behavior of the material at confining pressures from low to high. Specifically, the model effectively captures the softening response in the low-pressure region, represented by the 0 MPa and 3.4 MPa curves. The transition from brittle to ductile, strain hardening behavior at higher confining pressures is also satisfactorily captured. Fig. 7 (b) highlights the model's ability to reproduce the pressure-dependent stiffness exhibited by the material pre-yielding.

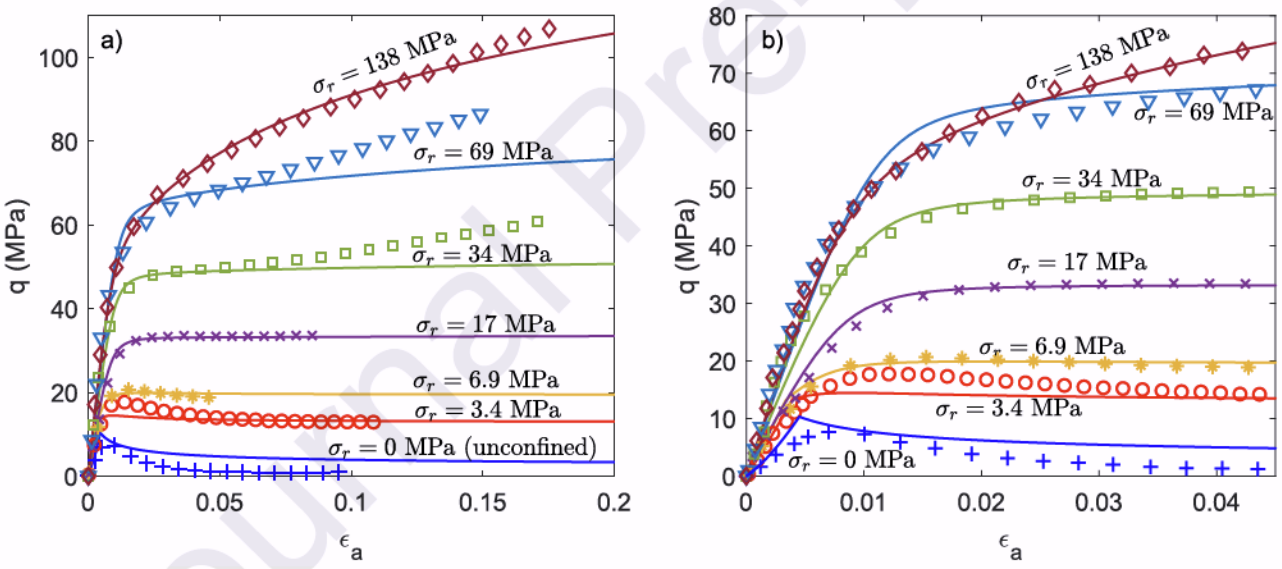

Figure 7: Model performance for confined compression behavior vs experimental data from Wiegand and Reddingius (2005) for PBS-9501 at the seven confining pressures ranging from 0 MPa to 138 MPa: (a) comparison for the whole axial strain range and (b) is a close up to 0.045 axial strain. Experimental data are depicted by scattered points, while the model is represented by a solid line.

As all granular materials experience significant volume change during shearing, it is worth to examine the predicted evolution of volumetric strain (Figure 8 (a)). Unfortunately, no corresponding volumetric experimental measurements were available for this dataset. One can see that the model predicts slight dilation under unconfined compression, while significant volumetric contraction under confinement with the magnitude increasing as the confining pressure rises. For crushable granular materials, volume

contraction at elevated confining pressures is commonly observed, as finer particles generated by grain crushing can fill the larger pore space to form more efficient packing.

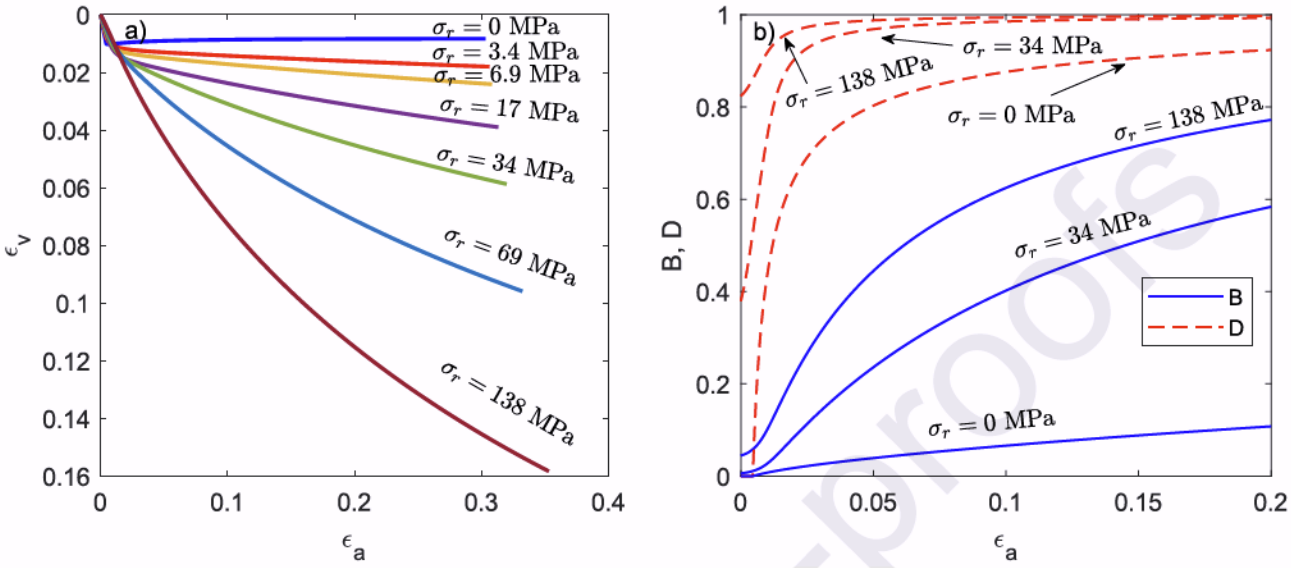

Figure 8: a) Model prediction for volumetric strain evolution for the different confining pressures; b) evolution for the breakage and damage internal variables for the 0, 34, and 138 MPa confining pressures obtained from model. Some of the curves do not start from zero which indicates that some breakage and damage has already occurred during the iso-compression stage.

Figure 8 (b) shows the evolution of the breakage and damage internal variables for the 0 MPa, 34 MPa, and 138 MPa curves. Both the breakage and damage values increase as the confining pressure rises. For the unconfined compression test, the breakage values remain relatively low (< 0.1) throughout the test, while damage accumulates rapidly at the beginning of loading and reaches a high value (0.9) at the end. This implies that the dominant micromechanism governing yielding and softening under unconfined compression is the debonding of the binder matrix, with minimal accompanying grain breakage events. For the 34 MPa and 138 MPa curves, significantly higher breakage values are predicted as increased confinement causes more pronounced grain crushing. The damage values for both tests exhibit a rapid increase during initial shearing, approaching 1, which signifies that cohesion is nearly depleted as the sample undergoes shearing until failure. In addition, it is worth noting that the damage and breakage values do not start from zero for the 34 MPa and 138 MPa cases. This is because the triaxial test includes an isotropic compression stage prior to shearing, inducing non-zero initial B and D values predicted by the model. This may not be physically correct as we expect that the plastic binder would not be significantly degraded under isotropic compression of the material (unless a large amount of gas voids is present in the matrix). X-ray images of isotropically compressed PBX samples may be helpful to validate this hypothesis. If necessary, the proposed model shall be refined to reduce (or even eliminate) damage growth under hydrostatic stresses.

The introduction of breakage internal variable allows us to track grain size distribution during loading. According to Eq. (1), determining the current cumulative GSD necessitates knowledge of two functions besides the current B value: the initial and the final cumulative GSDs. Given the unavailability of GSD data for PBS-9501, we opt to adopt the GSD data for PBX-9501 considering that PBS-9501 is

intended as a mock of PBX-9501. Previous studies have also shown similarities between sugar grains in PBS-9501 and HMX grains in PBX-9501 (Funk et al., 1996). The probability GSD by volume of PBX-9501 prior to shearing is given by Skidmore et al. (1998) and is presented in Figure 9 (a). The minimum and maximum grain diameters are approximately $1\,\mu$m and $1840\,\mu$m, respectively. To have a smooth representation of this GSD, three log-normal basis functions are used to fit the data

$$p(d) = \frac{1}{wd\sqrt{2\pi}} e^{\frac{-1}{2}\left(\frac{\ln(d)-\mu}{w}\right)^2} \tag{31}$$

where $p(d)$ is the volume percentage distribution, d is the grain diameter, μ is the mean, and w represents the width of the base function. To obtain a good fit for the initial experimental GSD, the following steps are taken: Firstly, the experimental probability GSD by Skidmore et al. (1998) was normalized such that the enclosing area equals to 1 (the original data yields an area much higher than 1, which we believe was a reporting error). Secondly, the mean (μ) and width (w) parameters of the three basis functions, together with their weighting factors were chosen in such a way to ensure the total area underneath equals to 1 and also best matches the experimental GSD. The final values of μ, w, and weighting factors are provided in Table 2. The resulting weighted basis function and the GSD curve are shown in Figure 9 (a). The cumulative GSD can be obtained through integration $F_i^g = \int_{d_{\min}^g}^{d_{\max}^g} p_i^g(d^g)\mathrm{d}d^g$, and is shown in Figure 9 (b). Since the ultimate cumulative GSD for PBS-9501 or PBX-9501 is not explicitly provided, we assume that it follows a fractal distribution (Einav, 2007a)

$$F_u(d) = \frac{d^{g(3-\alpha_u)} - d_{min}^{g\ (3-\alpha_u)}}{d_{\max}^{g\ (3-\alpha_u)} - d_{min}^{g\ (3-\alpha_u)}} \tag{32}$$

with fractal dimension $\alpha_u = 2.6$, minimum diameter ($d_{\min}^g$) of 1 μm, and maximum diameter ($d_{\max}^g$) of 250 μm. The hypothesized ultimate cumulative GSD is shown in Figure 9 (b). The predicted GSD evolution of PBS-9501 under 0 and 138 MPa confining pressures are shown in Figure 10 (a) and (b), respectively. One can see that progressive breakage leads to a redistribution of grain sizes, resulting in a more even distribution across the range of grain diameters. The GSD for unconfined compression almost stays the same because of the relatively low B values throughout loading. The prediction is intuitively sensible as reduced confining pressure reduces the average contact forces on individual grains and thus reduces crushing probability. Although no GSD data are available from Wiegand and Reddingius (2005) for comparison, we have planned new experimental campaigns on mock PBX involving thermal triaxial testing and X-ray imaging for a comprehensive validation and assessment of the model's predictive capability.

Table 2: Parameters for the basis functions for matching the initial GSD from Skidmore et al. (1998).

Basis #	μ (μm)	w (μm)	Weight

1	3.1	0.6	0.0338
2	4.1	0.4	0.0311
3	5.3	0.5	0.9351

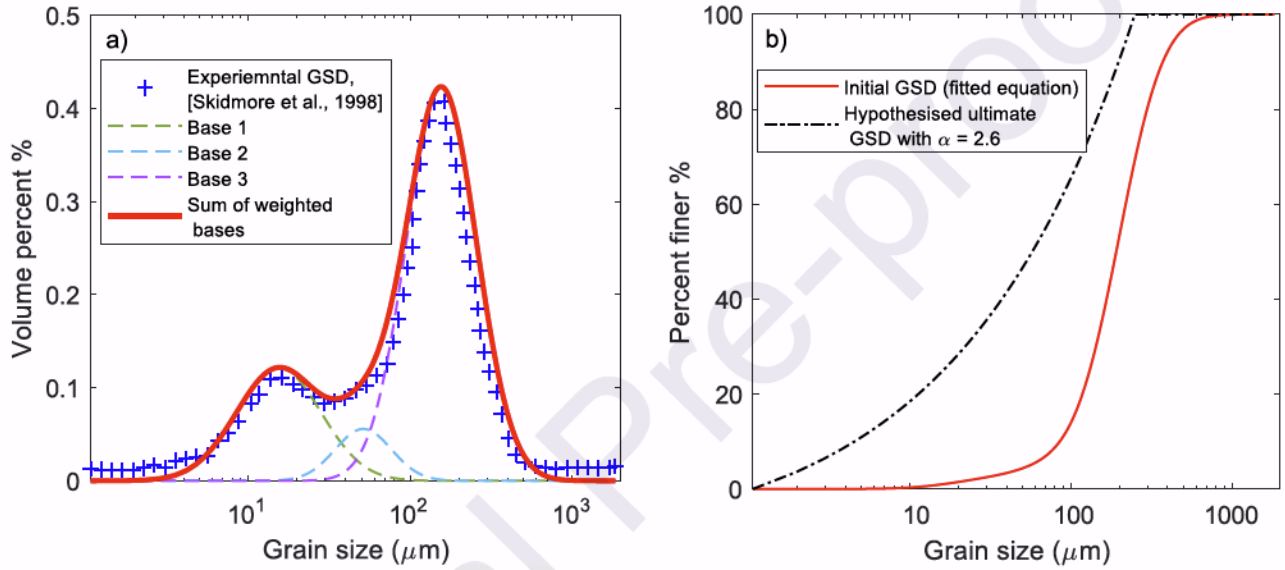

Figure 9: a) Fitting of GSD for PBX-9501 from Skidmore et al. (1998) using three weighted basis functions and their summation; b) initial cumulative GSD using the fitting equation and the hypothesized ultimate cumulative GSD.

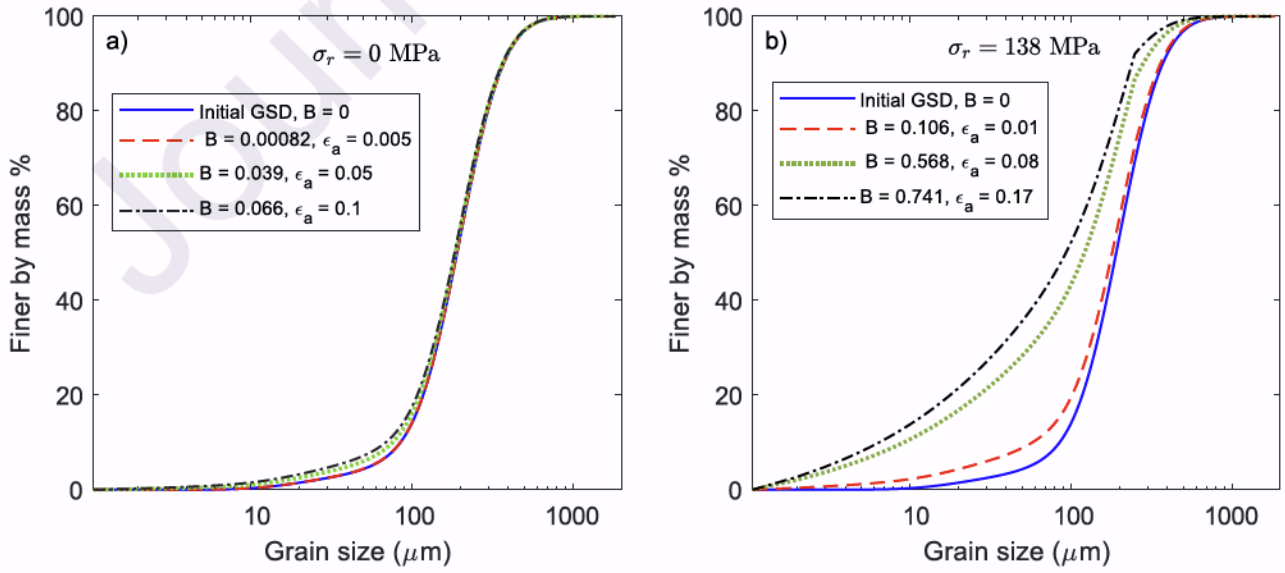

Figure 10: Predicted grain size distribution for a) unconfined compression curve and b) the 138 MPa confining pressure case. Corresponding axial strain values are indicated for each breakage value.

4.2. Quasi-static triaxial compression tests on CEA-M1 at high confining pressures

The second dataset is obtained from a series of triaxial compression tests conducted on CEA-M1, an HMX-based energetic material (Gruau et al., 2009), again at room temperature. The dataset consists of stress-strain responses obtained at much higher confining pressures compared to the PBX-9501 dataset: 100 MPa, 200 MPa, 400 MPa, and 800 MPa. Differing from the previous dataset, both axial and radial strains were measured during these experiments, providing a more comprehensive representation of the stress-strain response of PBXs. Figure 11 presents the modeled and the experimentally measured deviatoric stress (q) and the axial and radial strains for the four confining pressure values (model parameters used are listed in Table 1). The overall agreement between the two is satisfactory.

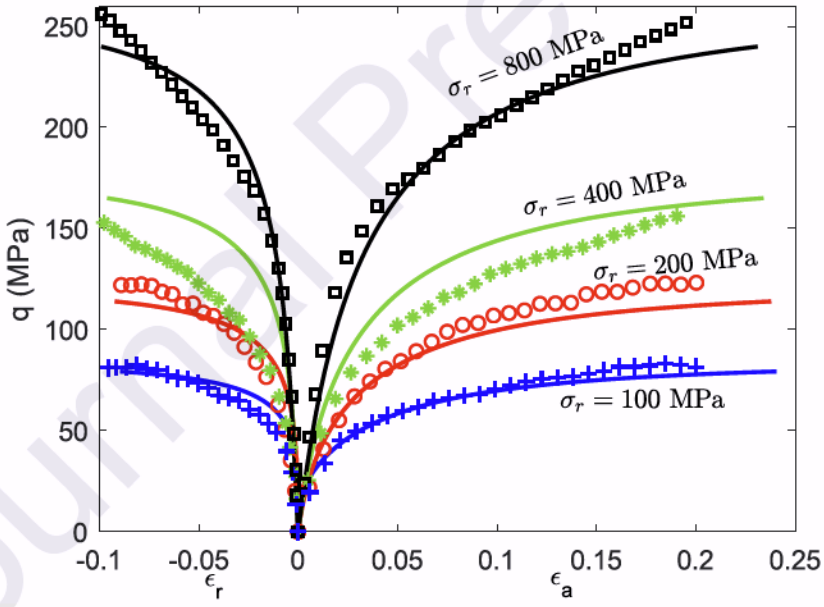

Figure 11: Comparison between experiments data (Gruau et al., 2009) and modeling results for triaxial compression tests on CEA-M1 samples.

4.3. Temperature-dependent behavior of PBXN-9 and PBX-9501

Most thermal-mechanical tests on PBX are conducted at different initial temperatures T_0, but with the temperature held constant throughout the test (i.e., dT=0), which is still classified as isothermal condition. Under this special condition, all the (T-T_0) terms in the constitutive relations (21)-(24) reduce to zero as in Sections 4.1 and 4.2, but one cannot assume the model parameters are still the same for each T_0 values.

We shall constrain the temperature-dependency of the material properties by physical arguments and past experimental observations.

1) Experimental studies conducted on pure energetic material grains and polymeric binders have revealed that the elastic modulus of both materials varies with temperature (Cady et al., 2006; Cui et al., 2010; Gallagher et al., 2015; Li et al., 2020; Pereverzev and Sewell, 2020; Quansah et al., 2022). Consequently, we will incorporate temperature dependency into the elastic parameters of both the grains and binder in the model, i.e., $\overline{K}^g$, G^g, K^b, and G^b. For simplification, we constrain the relationship between the binder bulk modulus (K^b) and binder shear modulus (G^b) by the linear elastic relation $G^b = \frac{3(1-2\nu)}{2(1+\nu)} K^b$, where the Poisson's ratio is assumed to be temperature independent and can take typical values from 0.3 to 0.49.
2) As temperature increases, the peak strength of PBX observed in the stress-strain curve decreases (Clements, 2011; Funk et al., 1996; Yeager et al., 2018). It is also well known that the cohesive properties of pure polymeric materials becomes weaker as the temperature increases (Cady et al., 2006). In the current model, the strength of both the grains and binder is controlled by three parameters: the critical breakage energy (E_{BC}), the critical damage energy (E_{DC}), and cohesion (c). Therefore, these parameters shall be formulated as functions of temperature.

In total, we consider six parameters (three elastic parameters $\overline{K}^g$, G^g, and K^b, and three dissipation parameters E_{BC}, E_{DC}, and c) to be temperature-dependent. Other parameters such as M^*, ω, and s could also be affected by temperature, but we regard these effects as of second-order importance to the stiffness and strength of PBX.

The relation between elastic properties and temperature, in principle, could be theoretically derived based on molecular-level arguments such (Anderson, 1966; Mahieux and Reifsnider, 2001). The dependency of critical energies E_{BC} and E_{DC} on T may be fundamentally rooted in the temperature-dependent fracture toughness (or surface energy) of the composing materials. Zhang and Buscarnera (2018) has outlined an upscaling strategy to explain how the environment (humidity and temperature) can affect the surface energy of the mineral and thus alter the global crushing resistance of the granular assembly. Finally, the thermal effect on apparent cohesion of the binder can be theorized based on energy arguments. One of the early models for predicting yield stress is the Eyring model, where it is assumed that polymer chain segments need to overcome an energy barrier at the yield point (Eyring, 1936; Gueguen et al., 2008). Another one is the cooperative model introduced by Fotheringham and Cherry (Fotheringham and Cherry, 1978; Fotheringham et al., 1976), which enhanced the Eyring equation by introducing an internal stress factor reflecting the material's thermal history, and it also included the effect of activation volume in the yield process (Richeton et al., 2005). Despite these exciting opportunities to bring fundamental thermal physics into the current constitutive framework, we opt to phenomenologically capture the temperature dependency limited by the scope of the current paper. The following procedure is adopted: we begin by calibrating the model using a response curve obtained at the lowest temperature. Typically, this temperature is below the glass transition temperature of the binder, where the binder behaves in a brittle manner. Once the curve at the lowest temperature is matched, the six identified temperature-dependent parameters are perturbed to best match other curves at higher temperatures. The

temperature dependency of these parameters is then established by plotting the obtained parameter values with respect to temperature (in Kelvin).

We choose two experimental datasets to examine the model performance at elevated temperatures. The first dataset (Clements, 2011) pertains to a PBX material called "PBXN-9" which is an actual explosive composed of 92 wt % HMX and 8 wt % binder (Glascoe et al., 2008). This dataset comprises unconfined compression tests conducted at four different temperatures: -40 °C, -15 °C, 23 °C, and 55 °C. The tests were carried out at a constant strain rate of 0.001/s. The model was initially calibrated at the lowest temperature of -40°C, and the corresponding parameter values were determined. Subsequently, the model was calibrated for the remaining temperatures while maintaining fixed values for parameters M^*, n, ω_B, ω_D, s_B, s_D, and ϑ across all curves. The performance of the model is shown in Figure 12 (a), and the calibrated parameters are summarized in Table 1. We see that the model matches the experimental stress-strain responses at different temperatures with great accuracy. The variation of the six temperature dependent parameters, i.e., $\overline{K}^g$, G^g, K^b, E_{BC}, E_{DC}, and c against temperature is shown in Figure 13. Exponential or power laws are chosen to fit for these parameters versus temperature data, as they always maintain positive when extrapolated to very high temperatures. On the other hand, using a linear equation, for example, could lead to unrealistic negative values at high temperatures. It is worth noting that the reduction of binder properties such as K^b, E_{DC}, and c at elevated temperatures reflects the intrinsic thermal-dependent properties of the polymeric binder. This should not be interpreted as the damage of the binder matrix which is captured separately by the damage ISV in the model formulation. Figure 12 (b) shows the model prediction of the temperature-dependent response using the fitting equations. Note that a certain degree of deviation is expected, as the fitting equations for the six parameters inherently introduce some variance from the actual parameters employed in Figure 12 (a).

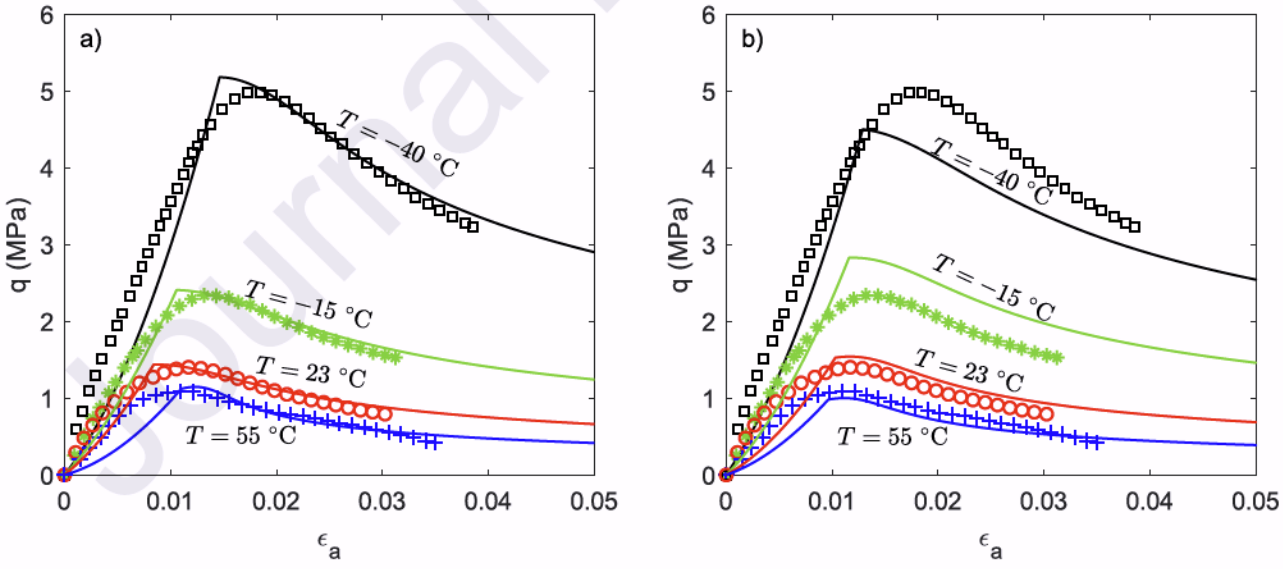

Figure 12: Model performance for temperature dependent behavior: a) model vs experimental data from Clements (2011) for PBXN-9 using the parameters listed in Table 1; b) model vs experimental data using the fitting equations for the temperature-dependent parameters. Experimental data are represented by scattered points, while the model predictions are depicted by a solid line.

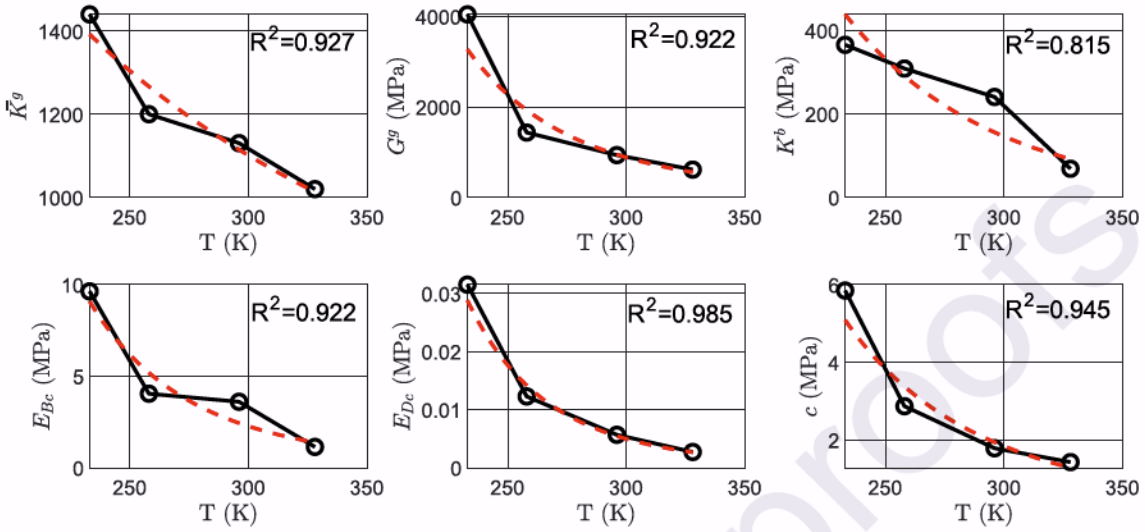

Figure 13: Fitting Equations for the temperature dependent parameters for the first data set in section 4.3. The parameters at the four different temperatures are represented in lined points in black while the corresponding fitting equation are in dashed red line. The fitting equation used for this data set are: $\bar{K}^g(T) = 2.2\times10^5 T^{-0.93}$; $G^g(T) = 5.77\times10^{15} T^{-5.17}$; $K^b(T) = 2\times10^4 e^{-0.02T}$; $E_{BC}(T) = 9.31\times10^{13} T^{-5.5}$; $E_{DC}(T) = 8.41\times10^{14} T^{-6.96}$; and $c(T) = 1.7\times10^{10} T^{-4.02}$.

The second dataset corresponds to PBX-9501 (Clements, 2011) under unconfined compression at three different temperatures: -10 °C, 25 °C, and 74 °C, with a strain rate of 0.1 /s. The parameters are calibrated through the same calibration procedure employed for PBXN-9 and are summarized in Table 1. Figure 14 (a) and (b) shows the model performance against the three curves at various temperatures during calibration and using the fitted equations, respectively. In summary, the model demonstrates its capability to accurately capture the stress-strain behavior at various temperature values. This is achieved by incorporating the temperature dependence of six model parameters, each possessing distinct and clear physical meanings.

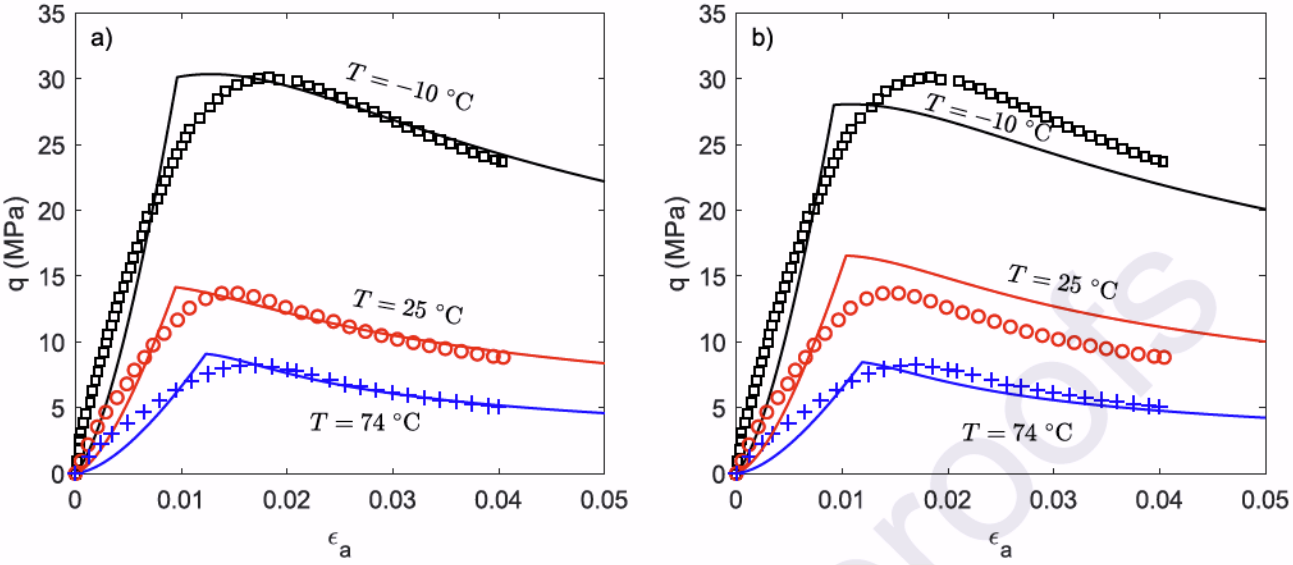

Figure 14: Model prediction for temperature dependent behavior: a) model vs experimental data for PBX-9501 (Clements, 2011) using the parameters listed in Table 1; b) model vs experimental data using the fitting equations for the temperature-dependent parameters. Experimental data are depicted as scattered points, while the model results are represented by a solid line. The fitting equations used for this data set are: $\bar{K}^g(T) = 9.25\times10^4 e^{-0.01T}$; $G^g(T) = 2.80\times10^{16}T^{-5.32}$; $K^b(T) = 5.75\times10^{26}T^{-9.69}$; $E_{BC}(T) = 1.25\times10^4 \mathrm{e}^{-0.03T}$; $E_{DC}(T) = 8.85\times10^{14}T^{-6.76}$; and $c(T) = 2.13\times10^{13}T^{-4.87}$.

4.4. Rate-dependent behavior of PBXN-9

Finally, we explore the capability of the model in capturing the rate-dependent behavior of PBX. The dataset used to assess the model is from unconfined compression tests on PBXN-9 conducted at three different strain rates which are: 0.0001 /s, 0.001 /s, and 0.01 /s under room temperature (23 °C) (Clements, 2011). The calibration process for this dataset follows a similar procedure as described in Section 3. The lowest strain rate (0.0001 /s) is selected as the "rate-independent" curve and is used to calibrate the rate-independent parameters (see Table 1). The two viscous parameters, namely η and m are then calibrated using the rate-dependent model to best match the stress-strain curves at higher strain rates (see Table 1). In Figure 15, it is observed that the rate-dependent model effectively captures the experimental data for all strain rates, although some deviations exist prior to yielding and in the softening regime. Specifically, the model predicts fixed stiffness in the elastic regime, while the experimental data exhibits a loading rate-dependent elasticity (i.e., viscoelasticity). This is because the current model primarily captures the viscoplastic behavior of the material, and no dissipation mechanism is active while the material is still within the elastic regime. The post-yielding softening response in the data exhibits a steeper decline compared to the model. This indicates that the actual sample experiences binder damage more rapidly under unconfined conditions than the current damage evolution law predicts. We believe that these mismatches are signals of overly stretching viscoplasticity to capture the rate sensitivity of the material which is likely a result of combined viscoelastic-viscoplastic properties. Once equipped with viscoelasticity features, the model should be able to handle the rate-dependent pre-peak behaviors at ease, giving plenty of flexibility for the viscoplasticity parameters to capture the peak and the post-peak responses. We plan to address these aspects in the future enhancements of the model.

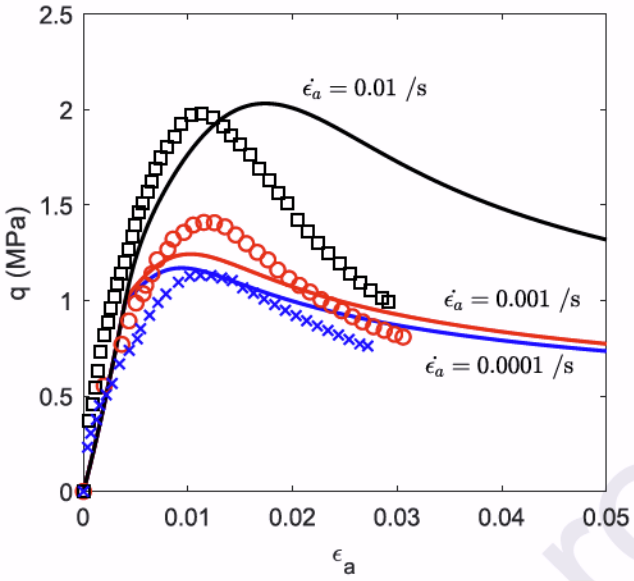

Figure 15: Comparison between the rate-dependent model and experimental data for PBXN-9 (Clements, 2011) at various strain rates. Experimental data are represented by scattered points, while the model results are depicted by a solid line.

5. Conclusions

We presented a non-isothermal breakage-damage mechanics theory for modeling the thermomechanical behavior of generic plastic-bonded granular materials. Given that PBMs are primarily composed of a polydisperse grain assembly bonded by a plastic binder matrix, breakage and damage internal state variables are introduced in the formulation to track the microstructural evolution of the material. The formulation takes temperature as a fundamental external variable and thus is sufficiently general to handle non-isothermal loading paths. Rate effects are realized through a Perzyna-type viscoplasticity formulation by adopting a non-homogeneous dissipation potential.

The performance of the model is assessed against multiple datasets obtained from various PBM or PBX samples subjected to confined and unconfined compression tests at different temperatures and strain rates. The proposed model can capture several key characteristics of PBM, including pressure-dependent elasticity, pressure-dependent failure, brittle-to-ductile transition, temperature dependency, and rate dependency in the post-yielding regime. In addition to stress-strain responses, the model tracks the evolution of breakage and damage variables throughout deformation, offering new avenues to validate and constrain the theory with experimental measurements. It is also observed that the model may overestimate the damage accumulation during isotropic compression, and is unable to capture the rate-dependent stiffness in the pre-yielding regime. Future extensions of the model may focus on refining the dissipation functions to reduce the damage under isotropic compression, implementing viscoelasticity, and accounting for localized deformation for treating the experiments as initial-boundary-value problems (IBVPs). In addition, a more comprehensive experimental datasets that contains volumetric strain and microstructural measurements (e.g., grain size distribution) at various pressures, temperatures, and strain rates for a consistent batch of PBM are desired to systematically validate the proposed theory and to inspire future improvements of the model.

CRediT authorship contribution statement

Yazeed Kokash: Data curation, Investigation, Methodology, Visualization, Writing – original draft. Richard Regueiro: Writing – review & editing. Nathan Miller: Writing – review & editing. Yida Zhang: Conceptualization, Methodology, Supervision, Writing – review & editing.

Declaration of competing interest

The authors declare that they have no known competing financial interests or personal relationships that could have appeared to influence the work reported in this paper.

Data availability

Data will be made available on request.

Acknowledgments

This research was supported by the Predictive Science Academic Alliance Program (PSAAP) under Award No. (DE-NA0003962) and the U.S. National Science Foundation (NSF) under NSF CMMI Award No. (2237332).

Appendix A. Derivation of the incremental constitutive relation

The incremental formulations of the mean and deviatoric stresses, breakage energy, damage energy and entropy are

$$\dot{p} = \frac{\partial p}{\partial \varepsilon_v^e}\dot{\varepsilon}_v^e + \frac{\partial p}{\partial \varepsilon_s^e}\dot{\varepsilon}_s^e + \frac{\partial p}{\partial B}\dot{B} + \frac{\partial p}{\partial D}\dot{D} + \frac{\partial p}{\partial T}\dot{T} \tag{A.1}$$

$$\dot{q} = \frac{\partial q}{\partial \varepsilon_v^e}\dot{\varepsilon}_v^e + \frac{\partial q}{\partial \varepsilon_s^e}\dot{\varepsilon}_s^e + \frac{\partial q}{\partial B}\dot{B} + \frac{\partial q}{\partial D}\dot{D} + \frac{\partial q}{\partial T}\dot{T} \tag{A.2}$$

$$\dot{E}_B = \frac{\partial E_B}{\partial \varepsilon_v^e}\dot{\varepsilon}_v^e + \frac{\partial E_B}{\partial \varepsilon_s^e}\dot{\varepsilon}_s^e + \frac{\partial E_B}{\partial T}\dot{T} \tag{A.3}$$

$$\dot{E}_D = \frac{\partial E_D}{\partial \varepsilon_v^e}\dot{\varepsilon}_v^e + \frac{\partial E_D}{\partial \varepsilon_s^e}\dot{\varepsilon}_s^e + \frac{\partial E_D}{\partial T}\dot{T} \tag{A.4}$$

$$\dot{S} = \frac{\partial S}{\partial \varepsilon_v^e}\dot{\varepsilon}_v^e + \frac{\partial S}{\partial \varepsilon_s^e}\dot{\varepsilon}_s^e + \frac{\partial S}{\partial B}\dot{B} + \frac{\partial S}{\partial D}\dot{D} + \frac{\partial S}{\partial T}\dot{T} \tag{A.5}$$

The elastic strain increment can be represented by total strain increment and plastic multiplier by consulting additive decomposition and flow rule:

$$\dot{\varepsilon}_v^e = \dot{\varepsilon}_v - \dot{\varepsilon}_v^p = \dot{\varepsilon}_v - \dot{\lambda}\frac{\partial \overline{y}}{\partial \overline{p}}; \dot{\varepsilon}_s^e = \dot{\varepsilon}_s - \dot{\varepsilon}_s^p = \dot{\varepsilon}_s - \dot{\lambda}\frac{\partial \overline{y}}{\partial \overline{q}}; \dot{B} = \dot{\lambda}\frac{\partial \overline{y}}{\partial \overline{E}_B}; \dot{D} = \dot{\lambda}\frac{\partial \overline{y}}{\partial \overline{E}_D} \tag{A.6}$$

Using Eq. (A.6), and enforcing the consistency condition, the plastic multiplier can be found as

$$\dot{\lambda} = \frac{\xi_v \dot{\varepsilon}_v + \xi_s \dot{\varepsilon}_s + \xi_T \dot{T}}{K_{PBD}} \tag{A.7}$$

where

$$\xi_v = (1-\vartheta B)\phi^g \left[\frac{\partial y}{\partial p}\frac{\partial^2 \psi_r^{\,g}}{\partial \varepsilon_v^{e2}} + \frac{\partial y}{\partial q}\frac{\partial^2 \psi_r^{\,g}}{\partial \varepsilon_v^e \partial \varepsilon_s^e}\right] + (1-D)\phi^b \left[\frac{\partial y}{\partial p}\frac{\partial^2 \psi_r^{\,b}}{\partial \varepsilon_v^{e2}} + \frac{\partial y}{\partial q}\frac{\partial^2 \psi_r^{\,b}}{\partial \varepsilon_v^e \partial \varepsilon_s^e}\right] + \vartheta\phi^g \frac{\partial y}{\partial E_B}\frac{\partial \psi_r^{\,g}}{\partial \varepsilon_v^e} + \phi^b \frac{\partial y}{\partial E_D}\frac{\partial \psi_r^{\,b}}{\partial \varepsilon_v^e} \tag{A.8}$$

$$\xi_s = (1-\vartheta B)\phi^g \left[\frac{\partial y}{\partial p}\frac{\partial^2 \psi_r^{\,g}}{\partial \varepsilon_v^e \partial \varepsilon_s^e} + \frac{\partial y}{\partial q}\frac{\partial^2 \psi_r^{\,g}}{\partial \varepsilon_s^{e2}}\right] + (1-D)\phi^b \left[\frac{\partial y}{\partial p}\frac{\partial^2 \psi_r^{\,b}}{\partial \varepsilon_v^e \partial \varepsilon_s^e} + \frac{\partial y}{\partial q}\frac{\partial^2 \psi_r^{\,b}}{\partial \varepsilon_s^{e2}}\right] + \vartheta\phi^g \frac{\partial y}{\partial E_B}\frac{\partial \psi_r^{\,g}}{\partial \varepsilon_s^e} + \phi^b \frac{\partial y}{\partial E_D}\frac{\partial \psi_r^{\,b}}{\partial \varepsilon_s^e} \tag{A.9}$$

$$\xi_B = \vartheta\phi^g \left(\frac{\partial y}{\partial p}\frac{\partial \psi_r^{\,g}}{\partial \varepsilon_v^e} + \frac{\partial y}{\partial q}\frac{\partial \psi_r^{\,g}}{\partial \varepsilon_s^e}\right) - \frac{\partial y}{\partial B} \tag{A.10}$$

$$\xi_D = \phi^b \left(\frac{\partial y}{\partial p}\frac{\partial \psi_r^{\,b}}{\partial \varepsilon_v^e} + \frac{\partial y}{\partial q}\frac{\partial \psi_r^{\,b}}{\partial \varepsilon_s^e}\right) - \frac{\partial y}{\partial D} \tag{A.11}$$

$$\xi_T = (1-\vartheta B)\phi^g \left[\frac{\partial y}{\partial p}\frac{\partial^2 \psi_r^{\,g}}{\partial \varepsilon_v^e \partial T} + \frac{\partial y}{\partial q}\frac{\partial^2 \psi_r^{\,g}}{\partial \varepsilon_s^e \partial T}\right] + \vartheta\phi^g \frac{\partial y}{\partial E_B}\frac{\partial \psi_r^{\,g}}{\partial T} + (1-D)\phi^b \left[\frac{\partial y}{\partial p}\frac{\partial^2 \psi_r^{\,b}}{\partial \varepsilon_v^e \partial T} + \frac{\partial y}{\partial q}\frac{\partial^2 \psi_r^{\,b}}{\partial \varepsilon_s^e \partial T}\right] + \phi^b \frac{\partial y}{\partial E_D}\frac{\partial \psi_r^{\,b}}{\partial T} + \frac{\partial y}{\partial T} \tag{A.12}$$

$$K_{PBD} = \frac{\partial \overline{y}}{\partial \overline{p}}\xi_v + \frac{\partial \overline{y}}{\partial \overline{q}}\xi_s + \frac{\partial \overline{y}}{\partial \overline{E}_B}\xi_B + \frac{\partial \overline{y}}{\partial \overline{E}_D}\xi_D \tag{A.13}$$

Substituting Eqs. (A.6) and (A.7) in Eqs. (A.1), (A.2), and (A.5), we get the following for the stresses and entropy increments and arranged in matrix from

$$\begin{pmatrix} \dot{p} \\ \dot{q} \\ \dot{S} \end{pmatrix} = \left[\mathbf{D}^e - \mathbf{D}^p - \mathbf{D}^B - \mathbf{D}^D\right] \begin{pmatrix} \dot{\varepsilon}_v \\ \dot{\varepsilon}_s \\ \dot{T} \end{pmatrix} \tag{A.14}$$

where

$$D^e = \begin{bmatrix} \alpha_{gb}^{vv} & \alpha_{gb}^{vs} & \alpha_{gb}^{vT} \\ \alpha_{gb}^{vs} & \alpha_{gb}^{ss} & \alpha_{gb}^{sT} \\ \alpha_{gb}^{vT} & \alpha_{gb}^{sT} & \alpha_{gb}^{TT} \end{bmatrix} \tag{A.15}$$

$$D^p = \frac{1}{K_{PBD}} \begin{bmatrix} \left(\frac{\partial \overline{y}}{\partial \overline{p}}\alpha_{gb}^{vv} + \frac{\partial \overline{y}}{\partial \overline{q}}\alpha_{gb}^{vs}\right)\xi_v & \left(\frac{\partial \overline{y}}{\partial \overline{p}}\alpha_{gb}^{vv} + \frac{\partial \overline{y}}{\partial \overline{q}}\alpha_{gb}^{vs}\right)\xi_s & \left(\frac{\partial \overline{y}}{\partial \overline{p}}\alpha_{gb}^{vv} + \frac{\partial \overline{y}}{\partial \overline{q}}\alpha_{gb}^{vs}\right)\xi_T \\ \left(\frac{\partial \overline{y}}{\partial \overline{p}}\alpha_{gb}^{vs} + \frac{\partial \overline{y}}{\partial \overline{q}}\alpha_{gb}^{ss}\right)\xi_v & \left(\frac{\partial \overline{y}}{\partial \overline{p}}\alpha_{gb}^{vs} + \frac{\partial \overline{y}}{\partial \overline{q}}\alpha_{gb}^{ss}\right)\xi_s & \left(\frac{\partial \overline{y}}{\partial \overline{p}}\alpha_{gb}^{vs} + \frac{\partial \overline{y}}{\partial \overline{q}}\alpha_{gb}^{ss}\right)\xi_T \\ \left(\frac{\partial \overline{y}}{\partial \overline{p}}\alpha_{gb}^{vT} + \frac{\partial \overline{y}}{\partial \overline{q}}\alpha_{gb}^{sT}\right)\xi_v & \left(\frac{\partial \overline{y}}{\partial \overline{p}}\alpha_{gb}^{vT} + \frac{\partial \overline{y}}{\partial \overline{q}}\alpha_{gb}^{sT}\right)\xi_s & \left(\frac{\partial \overline{y}}{\partial \overline{p}}\alpha_{gb}^{vT} + \frac{\partial \overline{y}}{\partial \overline{q}}\alpha_{gb}^{sT}\right)\xi_T \end{bmatrix} \tag{A.16}$$

$$D^B = \frac{\vartheta \phi^g}{K_{PBD}} \frac{\partial \overline{y}}{\partial \overline{\overline{E}}_B} \begin{bmatrix} \frac{\partial \psi_r^{\,g}}{\partial \varepsilon_v^e}\xi_v & \frac{\partial \psi_r^{\,g}}{\partial \varepsilon_v^e}\xi_s & \frac{\partial \psi_r^{\,g}}{\partial \varepsilon_v^e}\xi_T \\ \frac{\partial \psi_r^{\,g}}{\partial \varepsilon_s^e}\xi_v & \frac{\partial \psi_r^{\,g}}{\partial \varepsilon_s^e}\xi_s & \frac{\partial \psi_r^{\,g}}{\partial \varepsilon_s^e}\xi_T \\ \frac{\partial \psi_r^{\,g}}{\partial T}\xi_v & \frac{\partial \psi_r^{\,g}}{\partial T}\xi_s & \frac{\partial \psi_r^{\,g}}{\partial T}\xi_T \end{bmatrix} \tag{A.17}$$

$$D^D = \frac{\phi^b}{K_{PBD}} \frac{\partial \overline{y}}{\partial \overline{\overline{E}}_D} \begin{bmatrix} \frac{\partial \psi_r^{\,b}}{\partial \varepsilon_v^e}\xi_v & \frac{\partial \psi_r^{\,b}}{\partial \varepsilon_v^e}\xi_s & \frac{\partial \psi_r^{\,b}}{\partial \varepsilon_v^e}\xi_T \\ \frac{\partial \psi_r^{\,b}}{\partial \varepsilon_s^e}\xi_v & \frac{\partial \psi_r^{\,b}}{\partial \varepsilon_s^e}\xi_s & \frac{\partial \psi_r^{\,b}}{\partial \varepsilon_s^e}\xi_T \\ \frac{\partial \psi_r^{\,b}}{\partial T}\xi_v & \frac{\partial \psi_r^{\,b}}{\partial T}\xi_s & \frac{\partial \psi_r^{\,b}}{\partial T}\xi_T \end{bmatrix} \tag{A.18}$$

$$
\begin{aligned}
\alpha_{gb}^{vv} &= (1-\vartheta B)\phi^g \frac{\partial^2 \psi_r^{\ g}}{\partial \varepsilon_v^{e2}} + (1-D)\phi^b \frac{\partial^2 \psi_r^{\ b}}{\partial \varepsilon_v^{e2}} \\
\alpha_{gb}^{vs} &= (1-\vartheta B)\phi^g \frac{\partial^2 \psi_r^{\ g}}{\partial \varepsilon_v^e \partial \varepsilon_s^e} + (1-D)\phi^b \frac{\partial^2 \psi_r^{\ b}}{\partial \varepsilon_v^e \partial \varepsilon_s^e} \\
\alpha_{gb}^{vT} &= (1-\vartheta B)\phi^g \frac{\partial^2 \psi_r^{\ g}}{\partial \varepsilon_v^e \partial T} + (1-D)\phi^b \frac{\partial^2 \psi_r^{\ b}}{\partial \varepsilon_v^e \partial T} \\
\alpha_{gb}^{ss} &= (1-\vartheta B)\phi^g \frac{\partial^2 \psi_r^{\ g}}{\partial \varepsilon_s^{e2}} + (1-D)\phi^b \frac{\partial^2 \psi_r^{\ b}}{\partial \varepsilon_s^{e2}} \\
\alpha_{gb}^{sT} &= (1-\vartheta B)\phi^g \frac{\partial^2 \psi_r^{\ g}}{\partial \varepsilon_s^e \partial T} + (1-D)\phi^b \frac{\partial^2 \psi_r^{\ b}}{\partial \varepsilon_s^e \partial T} \\
\alpha_{gb}^{TT} &= (1-\vartheta B)\phi^g \frac{\partial^2 \psi_r^{\ g}}{\partial T^2} + (1-D)\phi^b \frac{\partial^2 \psi_r^{\ b}}{\partial T^2}
\end{aligned}
\tag{A.19}
$$

References

Addessio, F.L., Johnson, J.N., 1990. A constitutive model for the dynamic response of brittle materials. Journal of Applied Physics 67, 3275-3286.

Anderson, O.L., 1966. Derivation of Wachtman's equation for the temperature dependence of elastic moduli of oxide compounds. Physical Review 144, 553.

Bazant, Z.P., Belytschko, T.B., Chang, T.-P., 1984. Continuum theory for strain-softening. Journal of Engineering Mechanics 110, 1666-1692.

Bennett, J.G., Haberman, K.S., Johnson, J.N., Asay, B.W., 1998. A constitutive model for the non-shock ignition and mechanical response of high explosives. Journal of the Mechanics and Physics of Solids 46, 2303-2322.

Blumenthal, W., Gray III, G., Idar, D., Holmes, M., Scott, P., Cady, C., Cannon, D., 2000. Influence of temperature and strain rate on the mechanical behavior of PBX 9502 and Kel-F 800™, Aip conference proceedings. American Institute of Physics, pp. 671-674.

Bryant, E., Miller, N., Bennett, K., 2023. An extended three-field principle to scale-bridge the granular micromechanics of polymer-bonded particulate materials. Computer Methods in Applied Mechanics and Engineering 416, 116315.

Buechler, M.A., 2012. Viscoelastic-viscoplastic combined hardening constitutive model based on the Drucker Prager yield and flow potentials. Los Alamos National Lab.(LANL), Los Alamos, NM (United States).

Buechler, M.A., 2013a. A viscoelastic viscoplastic damage model. Los Alamos National Lab.(LANL), Los Alamos, NM (United States).

Buechler, M.A., 2013b. Viscoelastic viscoplastic damage model development, parameter estimation, and comparison to PBX9501 experimental data. Los Alamos National Lab.(LANL), Los Alamos, NM (United States).

Cady, C., Blumenthal, W., Gray Iii, G., Idar, D., 2006. Mechanical properties of plastic ‐ bonded explosive binder materials as a function of strain ‐ rate and temperature. Polymer Engineering & Science 46, 812-819.

Cady, C., Liu, C., Rae, P., Lovato, M., 2009. Thermal and loading dynamics of energetic materials, Proceedings of the Society of Experimental Mechanics Annual Conference. Society of Experimental Mechanics Bethel, Connecticu.

Caliez, M., Gratton, M., Frachon, A., Benelfellah, A., Picart, D., 2014. Viscoelastic plastic model and experimental validation for a granular energetic material. International journal of energetic materials and chemical propulsion 13.

Cil, M., Hurley, R., Graham-Brady, L., 2020. Constitutive model for brittle granular materials considering competition between breakage and dilation. Journal of Engineering Mechanics 146, 04019110.

Clements, B., 2011. ViscoSCRAM HE model developments. Los Alamos National Laboratory, United States.

Clements, B., Mas, E., 2004. A theory for plastic-bonded materials with a bimodal size distribution of filler particles. Modelling and Simulation in Materials Science and Engineering 12, 407.

Collins-Craft, N.A., Stefanou, I., Sulem, J., Einav, I., 2020. A Cosserat Breakage Mechanics model for brittle granular media. Journal of the Mechanics and Physics of Solids 141, 103975.

Cui, H.-L., Ji, G.-F., Chen, X.-R., Zhang, Q.-M., Wei, D.-Q., Zhao, F., 2010. Phase transitions and mechanical properties of octahydro-1, 3, 5, 7-tetranitro-1, 3, 5, 7-tetrazocine in different crystal phases by molecular dynamics simulation. Journal of Chemical & Engineering Data 55, 3121-3129.

Das, A., Nguyen, G.D., Einav, I., 2011. Compaction bands due to grain crushing in porous rocks: a theoretical approach based on breakage mechanics. Journal of Geophysical Research: Solid Earth 116.

Das, A., Nguyen, G.D., Einav, I., 2013. The propagation of compaction bands in porous rocks based on breakage mechanics. Journal of Geophysical Research: Solid Earth 118, 2049-2066.

Das, A., Tengattini, A., Nguyen, G.D., Viggiani, G., Hall, S.A., Einav, I., 2014. A thermomechanical constitutive model for cemented granular materials with quantifiable internal variables. Part II–validation and localization analysis. Journal of the Mechanics and Physics of Solids 70, 382-405.

Dienes, J., 1996. A unified theory of flow, hot spots, and fragmentation with an application to explosive sensitivity. High-Pressure Shock Compression of Solids II: Dynamic Fracture and Fragmentation, 366-398.

Dienes, J., Zuo, Q., Kershner, J., 2006. Impact initiation of explosives and propellants via statistical crack mechanics. Journal of the Mechanics and Physics of Solids 54, 1237-1275.

Dienes, J.K., 1978. A statistical theory of fragmentation, 19th US Symposium on Rock Mechanics (USRMS). OnePetro.

Dienes, J.K., 1985. A statistical theory of fragmentation processes. Mechanics of Materials 4, 325-335.

Donaghe, R.T., Chaney, R.C., Silver, M.L., 1988. Advanced triaxial testing of soil and rock. ASTM International.

Einav, I., 2007a. Breakage mechanics—part I: theory. Journal of the Mechanics and Physics of Solids 55, 1274-1297.

Einav, I., 2007b. Breakage mechanics—Part II: Modelling granular materials. Journal of the Mechanics and Physics of Solids 55, 1298-1320.

Eyring, H., 1936. Viscosity, plasticity, and diffusion as examples of absolute reaction rates. The Journal of chemical physics 4, 283-291.

Ferranti Jr, L., Gagliardi, F.J., Cunningham, B.J., Vandersall, K., 2010. Measure of quasi-static toughness and fracture parameters for mock explosive and insensitive high explosive LX-17, Proceeding of the 14th International Detonation Symposium, Coeur d'Alene, Idaho, pp. 11-16.

Fotheringham, D., Cherry, B., 1978. The role of recovery forces in the deformation of linear polyethylene. Journal of materials science 13, 951-964.

Fotheringham, D., Cherry, B., Bauwens-Crowet, C., 1976. Comment on "the compression yield behaviour of polymethyl methacrylate over a wide range of temperatures and strain-rates". Journal of Materials Science 11, 1368-1371.

Funk, D.J., Laabs, G.W., Peterson, P.D., Asay, B.W., 1996. Measurement of the stress/strain response of energetic materials as a function of strain rate and temperature: PBX 9501 and Mock 9501, AIP Conference Proceedings. American Institute of Physics, pp. 145-148.

Gagliardi, F., Cunningham, B., 2009. Axial-torsion testing plastic-bonded explosives to failure. Lawrence Livermore National Lab.(LLNL), Livermore, CA (United States).

Gallagher, H.G., Miller, J.C., Sheen, D.B., Sherwood, J.N., Vrcelj, R.M., 2015. Mechanical properties of β-HMX. Chemistry Central Journal 9, 1-15.

Gen, M., Cheng, R., 1999. Genetic algorithms and engineering optimization. John Wiley & Sons.

Glascoe, E., Maienschein, J., Burnham, A., Koerner, J., Hsu, P., Wemhoff, A., 2008. PBXN-9 ignition kinetics and deflagration rates. Lawrence Livermore National Lab.(LLNL), Livermore, CA (United States).

Goldberg, D.E., Holland, J.H., 1988. Genetic Algorithms and Machine Learning. Machine Learning 3, 95-99.

Gonzalez-Gutierrez, J., Cano, S., Schuschnigg, S., Kukla, C., Sapkota, J., Holzer, C., 2018. Additive Manufacturing of Metallic and Ceramic Components by the Material Extrusion of Highly-Filled Polymers: A Review and Future Perspectives. Materials 11, 840.

Gratton, M., Gontier, C., Allah, S.R.F., Bouchou, A., Picart, D., 2009. Mechanical characterisation of a viscoplastic material sensitive to hydrostatic pressure. European Journal of Mechanics-A/Solids 28, 935-947.

Gray III, G., Blumenthal, W., Idar, D., Cady, C., 1998. Influence of temperature on the high-strain-rate mechanical behavior of PBX 9501, AIP conference proceedings. American Institute of Physics, pp. 583-586.

Gruau, C., Picart, D., Belmas, R., Bouton, E., Delmaire-Sizes, F., Sabatier, J., Trumel, H., 2009. Ignition of a confined high explosive under low velocity impact. International Journal of Impact Engineering 36, 537-550.

Gueguen, O., Richeton, J., Ahzi, S., Makradi, A., 2008. Micromechanically based formulation of the cooperative model for the yield behavior of semi-crystalline polymers. Acta Materialia 56, 1650-1655.

Houlsby, G.T., Puzrin, A.M., 2007. Principles of hyperplasticity: an approach to plasticity theory based on thermodynamic principles. Springer Science & Business Media.

Idar, D., Lucht, R., Straight, J., Scammon, R., Browning, R., Middleditch, J., Dienes, J., Skidmore, C., Buntain, G., 1998. Low amplitude insult project: PBX 9501 high explosive violent reaction experiments. Los Alamos National Lab.(LANL), Los Alamos, NM (United States).

Jensen, R., Blommer, E., Brown, B., 1981. An instrumented shotgun facility to study impact initiated explosive reactions, Proc, p. 301.

Jr, L.F., Gagliardi, F.J., Cunningham, B.J., Vandersall, K.S., 2011. Dynamic characterization of mock explosive material using reverse Taylor impact experiments, Experimental and Applied Mechanics, Volume 6: Proceedings of the 2010 Annual Conference on Experimental and Applied Mechanics. Springer, pp. 337-346.

Le, V.D., 2007. Modélisation et identification du comportement plastique visco-élastique endommageable d'un matériau agrégataire. Tours.

Le, V.D., Gratton, M., Caliez, M., Frachon, A., Picart, D., 2010. Experimental mechanical characterization of plastic-bonded explosives. Journal of materials science 45, 5802-5813.

Li, M.-y., Bai, L.-f., Shi, Y.-b., Sun, G.-a., Wang, F., Gong, J., Ju, X., 2020. The influence of temperature and component proportion on stability, sensitivity, and mechanical properties of LLM-105/HMX co-crystals via molecular dynamics simulation. Journal of Molecular Modeling 26, 1-10.

Liu, C., Cady, C.M., Rae, P.J., Lovato, M.L., 2010. On the quantitative measurement of fracture toughness in high explosive and mock materials. Los Alamos National Lab.(LANL), Los Alamos, NM (United States).

Liu, C., Rae, P.J., Cady, C.M., Lovato, M.L., 2011. Damage & fracture of high-explosive mock subject to cyclic loading, Mechanics of Time-Dependent Materials and Processes in Conventional and Multifunctional Materials, Volume 3: Proceedings of the 2011 Annual Conference on Experimental and Applied Mechanics. Springer, pp. 151-157.

Mahieux, C.A., Reifsnider, K.L., 2001. Property modeling across transition temperatures in polymers: a robust stiffness–temperature model. Polymer 42, 3281-3291.

Manner, V.W., Yeager, J.D., Patterson, B.M., Walters, D.J., Stull, J.A., Cordes, N.L., Luscher, D.J., Henderson, K.C., Schmalzer, A.M., Tappan, B.C., 2017. In situ imaging during compression of plastic bonded explosives for damage modeling. Materials 10, 638.

Miller, N.A., Regueiro, R.A., Shahabi, F., Bishop, J.E., 2022. A micromorphic filter for determining stress and deformation measures from direct numerical simulations of lower length scale behavior. International Journal for Numerical Methods in Engineering 123, 3879-3921.

Paterson, M.S., Wong, T.-f., 2005. Experimental rock deformation: the brittle field. Springer.

Pereverzev, A., Sewell, T., 2020. Elastic coefficients of β-HMX as functions of pressure and temperature from molecular dynamics. Crystals 10, 1123.

Perzyna, P., 1966. Fundamental problems in viscoplasticity. Advances in applied mechanics 9, 243-377.

Plassart, G., Picart, D., Gratton, M., Frachon, A., Caliez, M., 2020. Quasistatic mechanical behavior of HMX-and TATB-based plastic-bonded explosives. Mechanics of Materials 150, 103561.

Plassart, G., Picart, D., Gratton, M., Frachon, A., Caliez, M., 2022. Quasistatic anisotropic induced behaviour of a tatb-based plastic-bonded explosive. Mechanics of Materials 170, 104318.

Quansah, J.D., Zhang, X., Wasiullah, Q., Yan, Q., 2022. Mechanical and thermophysical properties of energetic crystals: evaluation methods and recent achievements. FirePhysChem.

Rae, P., Goldrein, H., Palmer, S., Field, J., Lewis, A., 2002. Quasi–static studies of the deformation and failure of β–HMX based polymer bonded explosives. Proceedings of the Royal Society of London. Series A: Mathematical, Physical and Engineering Sciences 458, 743-762.

Regueiro, R.A., 2010. On finite strain micromorphic elastoplasticity. International Journal of Solids and Structures 47, 786-800.

Richeton, J., Ahzi, S., Daridon, L., Rémond, Y., 2005. A formulation of the cooperative model for the yield stress of amorphous polymers for a wide range of strain rates and temperatures. Polymer 46, 6035-6043.

Rueda, M.M., Auscher, M.-C., Fulchiron, R., Périé, T., Martin, G., Sonntag, P., Cassagnau, P., 2017. Rheology and applications of highly filled polymers: A review of current understanding. Progress in Polymer Science 66, 22-53.

Shen, X., Buscarnera, G., 2022. A breakage–damage framework for porous granular rocks in surface-reactive environments. International Journal of Rock Mechanics and Mining Sciences 154, 105111.

Singh, S., Zurakowski, Z., Dai, S., Zhang, Y., 2021. Effect of Grain Crushing on the Hydraulic Conductivity of Tailings Sand. Journal of Geotechnical and Geoenvironmental Engineering 147, 04021143.

Skidmore, C., Phillips, D., Son, S., Asay, B., 1998. Characterization of HMX particles in PBX 9501, AIP Conference Proceedings. American Institute of Physics, pp. 579-582.

Tengattini, A., Das, A., Einav, I., 2016. A constitutive modelling framework predicting critical state in sand undergoing crushing and dilation. Géotechnique 66, 695-710.

Tengattini, A., Das, A., Nguyen, G.D., Viggiani, G., Hall, S.A., Einav, I., 2014. A thermomechanical constitutive model for cemented granular materials with quantifiable internal variables. Part I—Theory. Journal of the Mechanics and Physics of Solids 70, 281-296.

Trzaskowska, M., Vivcharenko, V., Franus, W., Goryczka, T., Barylski, A., Przekora, A., 2023. Optimization of the Composition of Mesoporous Polymer–Ceramic Nanocomposite Granules for Bone Regeneration. Molecules 28, 5238.

Wang, G., Zhang, S., Wang, Z., Cui, Q., 2022. Mechanical properties of DNAN/HMX melt-cast explosive. AIP Advances 12, 065227.

Wiegand, D., Reddingius, B., 2004. Mechanical properties of plastic bonded composites as a function of hydrostatic pressure, AIP Conference Proceedings. American Institute of Physics, pp. 812-815.

Wiegand, D.A., Reddingius, B., 2005. Mechanical properties of confined explosives. Journal of Energetic Materials 23, 75-98.

Wiegand, D.A., Redingius, B., Ellis, K., Leppard, C., 2011. Pressure and friction dependent mechanical strength–cracks and plastic flow. International journal of solids and structures 48, 1617-1629.

Wong, T.-f., Baud, P., 2012. The brittle-ductile transition in porous rock: A review. Journal of Structural Geology 44, 25-53.

Xu, W., Guo, F., Liang, X., Yan, T., Xu, Y., Deng, J., Li, Y., Wang, J., 2021. Dynamic response properties of polymer bonded explosives under different excitation by deceleration. Materials & Design 206, 109810.

Yeager, J.D., Woznick, C.S., Thompson, D.G., Duque, A.H., Liu, C., Burch, A.C., Bowden, P.R., Shorty, M., Bahr, D.F., 2018. Development of a new density and mechanical mock for HMX, Proceedings of the 16th international detonation symposium, Cambridge, pp. 1631-1641.

Zhang, X., Oskay, C., 2019. Plastic dissipation sensitivity to mechanical properties in polycrystalline β-HMX subjected to impact loading. Mechanics of Materials 138, 103079.

Zhang, Y., Buscarnera, G., 2017. A rate-dependent breakage model based on the kinetics of crack growth at the grain scale. Géotechnique 67, 953-967.

Zhang, Y., Buscarnera, G., 2018. Breakage mechanics for granular materials in surface-reactive environments. Journal of the Mechanics and Physics of Solids 112, 89-108.

Zubelewicz, A., Thompson, D.G., Ostoja-Starzewski, M., Ionita, A., Shunk, D., Lewis, M.W., Lawson, J.C., Kale, S., Koric, S., 2013. Fracture model for cemented aggregates. AIP Advances 3, 012119.

Declaration of competing interest

The authors declare that they have no known competing financial interests or personal relationships that could have appeared to influence the work reported in this paper.

Highlights

1- A micromechanics-based, thermodynamically consistent constitutive model is developed for plastic bonded granular materials (PBM).

2- The model can account for the breakage of the grains and the damage of the plastic binder matrix for PBMs under thermomechanical loadings.

3- The model successfully reproduces the temperature, pressure, and rate dependent behaviors of PBMs.